Remote control: the cancer cell-intrinsic mechanisms that dictate systemic inflammation and anti-tumor immunity

Wellenstein, M.D.

Loss of p53 triggers WNT-dependent systemic inflammation to drive breast cancer metastasis

Max D. Wellenstein[1, #], Seth B. Coffelt[1, 2, #], Danique E.M. Duits[1], Martine H. van Miltenburg[3], Maarten Slagter[4,5], Iris de Rink[6], Linda Henneman[7], Sjors M. Kas[3], Stefan Prekovic[8], Cheei-Sing Hau[1], Kim Vrijland[1], Anne Paulien Drenth[3], Renske de Korte-Grimmerink[7], Eva Schut[3], Ingrid van der Heijden[3], Wilbert Zwart[8], Lodewyk F.A. Wessels[5], Ton N. Schumacher[4], Jos Jonkers[3, *], Karin E. de Visser[1, *]

Nature. 2019 Aug;572(7770):538-542.
doi: 10.1038/s41586-019-1450-6.

Affiliations
[1] Division of Tumor Biology & Immunology, Oncode Institute, Netherlands Cancer Institute, 1066CX Amsterdam, The Netherlands; [2] Current address: Institute of Cancer Sciences, University of Glasgow and Cancer Research UK Beatson Institute, Glasgow G61 1BD, UK; [3] Division of Molecular Pathology, Oncode Institute, Netherlands Cancer Institute, 1066CX Amsterdam, The Netherlands; [4] Division of Molecular Oncology & Immunology, Oncode Institute, Netherlands Cancer Institute, 1066CX Amsterdam, The Netherlands; [5] Division of Molecular Carcinogenesis, Oncode Institute, Netherlands Cancer Institute, 1066CX Amsterdam, The Netherlands; [6] Genomics Core Facility, Netherlands Cancer Institute, 1066CX Amsterdam, The Netherlands; [7] Mouse Clinic for Cancer and Aging, Netherlands Cancer Institute, 1066CX Amsterdam, The Netherlands; [8] Division of Oncogenomics, Oncode Institute, Netherlands Cancer Institute, 1066CX Amsterdam, The Netherlands.

[#] These authors contributed equally

[*] Corresponding authors

Abstract

Cancer-associated systemic inflammation is strongly linked with poor disease outcome in cancer patients[1,2]. For most human epithelial tumor types, high systemic neutrophil-to-lymphocyte ratios are associated with poor overall survival[3], and experimental studies have demonstrated a causal relationship between neutrophils and metastasis[4,5]. However, the cancer cell-intrinsic mechanisms dictating the substantial heterogeneity in systemic neutrophilic inflammation between tumor-bearing hosts are largely unresolved. Using a panel of 16 distinct genetically engineered mouse models (GEMMs) for breast cancer, we have uncovered a novel role for cancer cell-intrinsic p53 as a key regulator of pro-metastatic neutrophils. Mechanistically, p53 loss in cancer cells induced secretion of WNT ligands that stimulate IL-1β production by tumor-associated macrophages, which drives systemic inflammation. Pharmacological and genetic blockade of WNT secretion in p53-null cancer cells reverses IL-1β expression by macrophages and subsequent neutrophilic inflammation, resulting in reduced metastasis formation. Collectively, we demonstrate a novel mechanistic link between loss of p53 in cancer cells, WNT ligand secretion and systemic neutrophilia that potentiates metastatic progression. These insights illustrate the importance of the genetic makeup of breast tumors in dictating pro-metastatic systemic inflammation, and set the stage for personalized immune intervention strategies for cancer patients.

Results & Discussion

To determine how pro-metastatic systemic inflammation is influenced by genetic aberrations in tumors, we studied 16 GEMMs for breast cancer carrying different tissue-specific mutations. These GEMMs represent most subtypes of human breast cancer, including ductal and lobular carcinoma, estrogen receptor-positive (luminal A), HER2$^+$, triple-negative and basal-like breast cancer. Because we and others have demonstrated that neutrophils expand systemically and promote metastasis[5-10], we evaluated circulating neutrophil levels as a marker for systemic inflammation in mammary tumor-bearing mice with end-stage disease. As expected, most tumor-bearing mice displayed an increase in circulating neutrophils as compared to non-tumor-bearing animals (wild-type [WT]) (**Fig. 3.1a**). Like the inter-patient heterogeneity in systemic inflammation in human breast cancer[11], we observed a striking variability in the extent of neutrophilia between the different tumor-bearing GEMMs (**Fig. 3.1a, Extended Data Fig. 3.1a**). We found that the models exhibiting high neutrophil expansion displayed a subset of neutrophils expressing the stem cell marker cKIT (**Fig. 3.1b**), indicative of an immature neutrophil phenotype[5]. We subsequently searched for commonalities and differences among the 16 GEMMs with regards to high versus low systemic neutrophil levels. Strikingly, mice bearing tumors with a p53 deletion exhibited the most pronounced circulating neutrophil levels (**Fig. 3.1a**). The difference in magnitude of systemic inflammation between p53-proficient and p53-null tumors was even more apparent when focusing on cKIT$^+$ neutrophils (**Fig. 3.1b**).

In mouse models for colorectal, pancreatic, prostate and endometrial cancer, p53 mutation or loss leads to recruitment and activation of immune cells in the primary tumor microenvironment[12-16]. To study the association between p53 status of the tumor and systemic inflammation, we separated the 16 GEMMs based on the presence or absence of homozygously floxed *Trp53* alleles and compared the levels of circulating neutrophils and the proportion of cKIT-expressing neutrophils. This analysis confirmed a statistically significant difference between mice bearing p53-proficient and p53-null tumors (**Fig. 3.1c, d**).

We previously demonstrated that expansion of neutrophils in mammary tumor-bearing *K14-cre;Cdh1$^{F/F}$;Trp53$^{F/F}$* (KEP) mice is driven by an inflammatory pathway involving CCL2, IL-1β, IL-17A and G-CSF[5,17]. We found that serum levels of CCL2, IL-1β and G-CSF correlated with p53 loss in primary tumors in the 16 GEMMs (**Fig. 3.1e–h**). Principal component analysis of these systemic immune parameters further demonstrated that systemic inflammation correlated with p53 status of the tumor (**Fig. 3.1i**).

To provide evidence for a causal relationship between p53-loss in mammary tumors and neutrophilia, we derived cancer cell lines from two independent p53-proficient tumor models, *Wap-cre;Cdh1$^{F/F}$;Akt^{E17K}* (WEA)[18] and *Wap-cre;Cdh1$^{F/F}$;Pik3ca^{E545K}* (WEP). Using CRISPR/Cas9-mediated gene disruption, we targeted *Trp53*, which resulted in an inability to increase p21 levels after irradiation (**Extended Data Fig. 3.2a, b, e**). We orthotopically transplanted *WEA;Trp53$^{+/+}$* and *WEP;Trp53$^{+/+}$* cells, and matched *WEA;Trp53$^{-/-}$* and *WEP;Trp53$^{-/-}$* cells into syngeneic WT mice (**Fig. 3.2a**). While p53-loss conferred a proliferation advantage *in vitro, in vivo* growth kinetics were similar between p53-proficient and -deficient tumors for both cell lines (**Extended Data Fig. 3.2c–g**). Consistent with our findings in the GEMM panel, we observed increased expansion of neutrophils, including cKIT$^+$ neutrophils, in the circulation and lungs of mice bearing *WEA;Trp53$^{-/-}$* and *WEP;Trp53$^{-/-}$* tumors, when compared to mice bearing size-matched p53-proficient tumors (**Fig. 3.2b–d, Extended Data Fig. 3.2h, i**). In

addition, mice with *WEA;Trp53*$^{-/-}$, but not *WEP;Trp53*$^{-/-}$ tumors, presented with splenomegaly when compared to *Trp53*$^{+/+}$ controls (**Extended Data Fig. 3.2j**), a phenomenon often observed in inflammation and cancer[19]. These data reveal that loss of p53 in breast cancer cells is a central driving event of cancer-induced systemic neutrophilic inflammation.

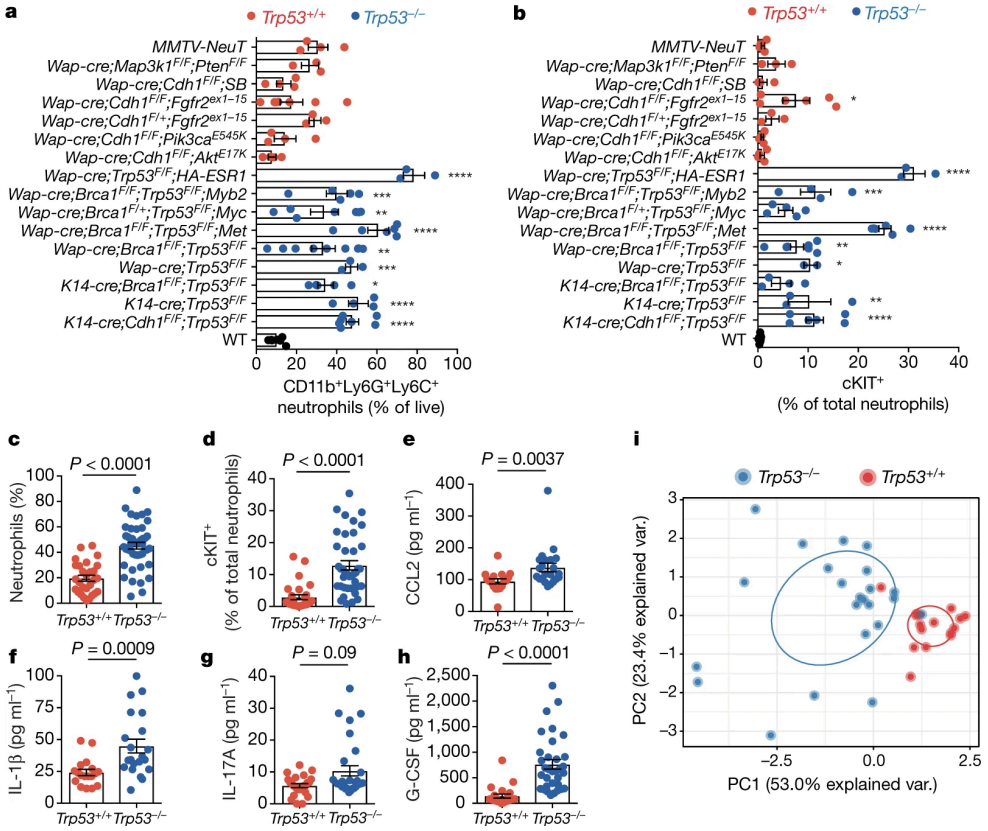

Figure 3.1: Loss of p53 in mammary cancer cells correlates with systemic neutrophilic inflammation. a. Flow cytometry analysis of frequency of CD11b$^+$Ly6G$^+$Ly6C$^+$ neutrophils and **b.** proportion of cKIT$^+$ neutrophils as determined by flow cytometry analysis on blood of breast cancer GEMMs at end-stage (cumulative tumor volume 1500 mm^3) and non-tumor-bearing (WT) controls (n=4, 3, 4, 7, 3, 4, 4, 3, 6, 7, 6, 9, 3, 5, 4, 7 and 7 mice, top to bottom). Asterisks indicate statistically significant differences compared to WT. * $P < 0.05$, ** $P < 0.01$, *** $P < 0.001$, **** $P < 0.0001$. **c.** Total neutrophil frequencies and **d.** cKIT$^+$ neutrophil frequencies in circulation of all *Trp53*$^{+/+}$ (n=28) and *Trp53*$^{-/-}$ (n=46) tumor-bearing mice, combined from **a.** and **b. e.** CCL2 levels (n=17 *Trp53*$^{+/+}$, n=22 *Trp53*$^{-/-}$), **f.** IL-1β levels (n=18 *Trp53*$^{+/+}$, n=21 *Trp53*$^{-/-}$), **g.** IL-17A levels (n=24 *Trp53*$^{+/+}$, n=30 *Trp53*$^{-/-}$) and **h.** G-CSF levels (n=22 *Trp53*$^{+/+}$, n=33 *Trp53*$^{-/-}$) in serum of GEMMs at end-stage based on p53 status. **i.** Principal component analysis of data depicted in **a** – **h** (13 out of 16 GEMMs)**.** Each symbol represents one mouse. Circles contour 40% of group-specific Gaussian probability distributions of sample scores. All data are means ± s.e.m., *P*-values are indicated as determined by two-tailed one-way ANOVA, Tukey's multiple-testing correction (**a, b**) or two-tailed Mann-Whitney U-test (**c – h**).

Since we observed cKIT+ immature neutrophils in p53-null tumor-bearing mice (**Fig. 3.1d, 3.2d**), we next investigated whether hematopoiesis was altered. In mice bearing *WEA;Trp53*$^{-/-}$ tumors, frequencies of Lin^{-}Sca1^{+}cKIT^{+} cells (LSKs), common myeloid progenitors (CMPs), CD11b^{+}Ly6G^{low} pro-myelocytes and mature neutrophils were increased in the bone marrow at the expense of megakaryocyte and erythrocyte progenitors (MEPs), when compared to *WEA;Trp53*$^{+/+}$ tumor-bearing mice (**Extended Data Fig. 3.3a–c**). This effect on cell proportions was not reflected in the total cell counts, possibly due to a slight depletion of total bone marrow cell numbers in *WEA;Trp53*$^{-/-}$ tumor-bearing mice (**Extended Data Fig. 3.3d**).

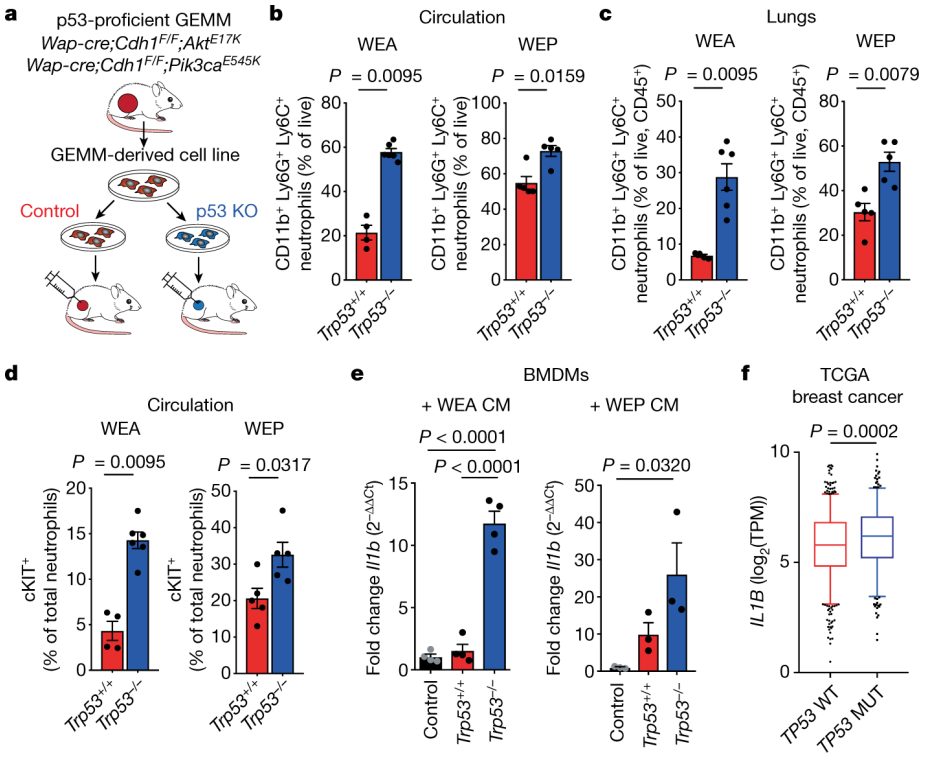

Figure 3.2. p53 status in mammary tumors dictates immune activation. a. Experimental setup: cell lines are derived from *Trp53*$^{+/+}$ tumors (*Wap-cre;Cdh1*$^{F/F}$*;Akt*^{E17K} (WEA) and *Wap-cre;Cdh1*$^{F/F}$*;Pik3ca*^{E545K} (WEP)) and p53 is knocked out (KO) using CRISPR/Cas9. KO and control cell lines are orthotopically transplanted into syngeneic mice. **b.** Frequency of total CD11b^{+}Ly6G^{+}Ly6C^{+} neutrophils in circulation and **c.** in lungs, and **d.** frequency of cKIT^{+} neutrophils (% of total neutrophils) in circulation at end-stage (tumor volume 1500 mm^3) of mice with *Trp53*$^{+/+}$ and *Trp53*$^{-/-}$ *WEA* and *WEP* tumors, as determined by flow cytometry (*n*=4 *WEA;Trp53*$^{+/+}$, *n*=6 *WEA;Trp53*$^{-/-}$, *n*=5 *WEP;Trp53*$^{+/+}$, *n*=5 *WEP;Trp53*$^{-/-}$). **e.** RT-qPCR analysis of the expression of *Il1b* in bone marrow-derived macrophages (BMDM) after exposure to conditioned medium from *Trp53*$^{+/+}$ and *Trp53*$^{-/-}$ *WEA* (*n*=4 biological replicates/group) or *WEP* cell lines (*n*=3 biological replicates/group). Plots show representative of 3 independent experiments with 2 technical replicates per biological replicate. **f.** *IL1B* expression in *TP53* wild-type (WT, *n*=643) or *TP53* mutant (MUT, *n*=351) human breast tumors of The Cancer Genome Atlas (TCGA) database. Data in **b** – **e** are means ± s.e.m., **f.** shows 5 – 95 percentile boxplot with median and quartiles indicated. *P*-values are indicated as determined by two-tailed Mann-Whitney U-test (**b, c, d, f**) or two-tailed one-way ANOVA, Tukey's multiple-testing correction (**e**).

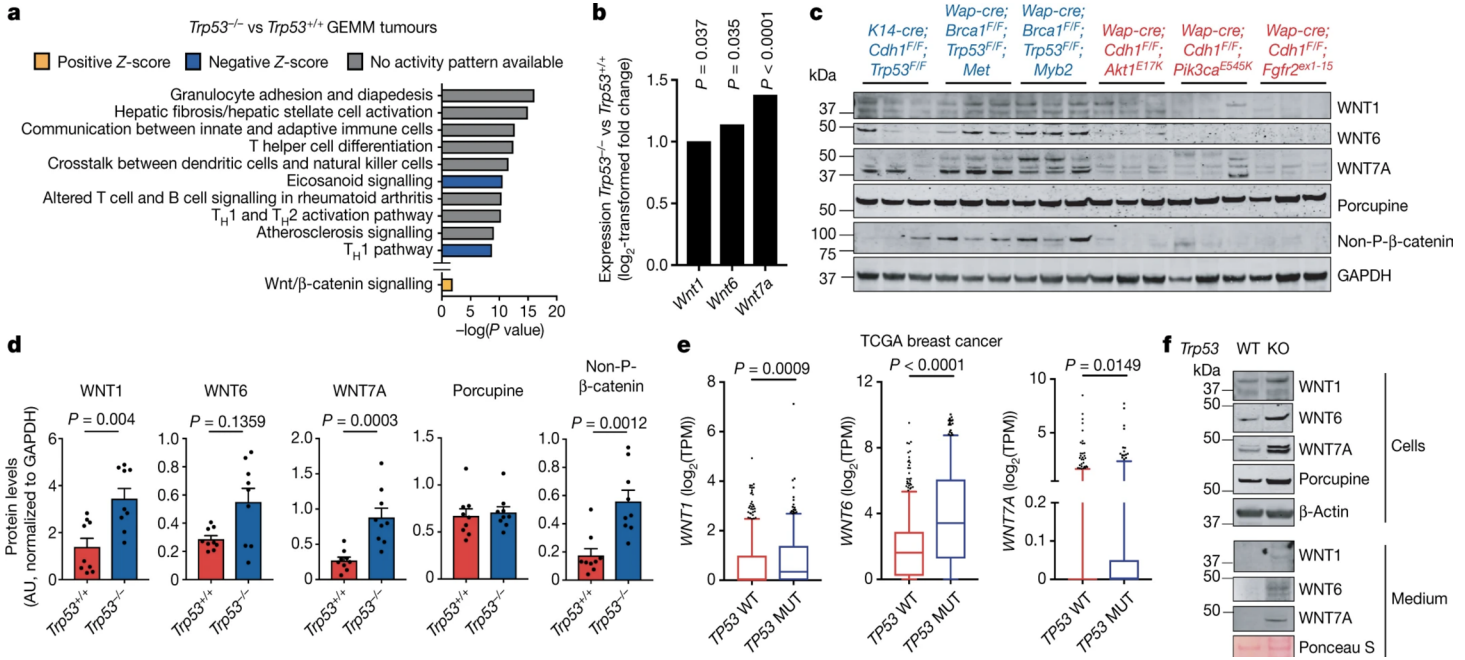

Figure 3.3. p53-null tumors display activated WNT signaling. a. Top 10 most significantly differentially activated pathways determined by Ingenuity Pathway Analysis, comparing *Trp53*$^{-/-}$ (*n*=77) with *Trp53*$^{+/+}$ (*n*=68) GEMM tumors of 12 different models. Also indicated is the WNT signaling pathway. **b.** Log_2 fold change expression of *Wnt1, Wnt6* and *Wnt7a* in *Trp53*$^{-/-}$ (*n*=77) GEMM tumors compared to *Trp53*$^{+/+}$ (*n*=68) tumors. **c.** Western blot analysis of bulk tumors showing non-phospho(active)-β-catenin, Porcupine, WNT1, WNT6 and WNT7a (blue indicates *Trp53*$^{-/-}$ tumors and red indicates *Trp53*$^{+/+}$ tumors). Representative of two independent experiments. For uncropped images, see Supplemental Fig. 1 (online). **d.** Quantification of **c** (*n*=3/group). **e.** Expression of *WNT1, WNT6* and *WNT7A* in *TP53* wild-type (WT, *n*=643) and *TP53* mutant (MUT, *n*=351) human breast tumors of TCGA breast cancer database. **f.** Western blot analysis on cell lysate and conditioned medium of *Wap-cre;Cdh1*$^{F/F}$*;Akt*^{E17K}*;Trp53*$^{+/+}$ (WT) and *Wap-cre;Cdh1*$^{F/F}$*;Akt*^{E17K}*;Trp53*$^{-/-}$ (KO) cell lines for WNT ligands. Representative of two independent experiments. **d.** shows mean ± s.e.m., **e** shows 5 – 95 percentile boxplot with median and quartiles indicated. *P*-values are indicated as determined by two-tailed one-way ANOVA, FDR multiple-testing correction (**b**) or two-tailed Mann-Whitney U-test (**d, e**).

Previously, we reported that macrophage-derived IL-1β in the tumor microenvironment triggers systemic neutrophil expansion in KEP mice[5]. Since IL-1β serum levels correlated with p53 status (**Fig. 3.1f**) we hypothesized that loss of p53 changes the secretome of cancer cells, stimulating IL-1β production from tumor-associated macrophages (TAMs) and setting off a systemic inflammatory cascade. Indeed, *in vitro* exposure of bone marrow-derived macrophages (BMDMs) to conditioned medium (CM) from *WEA;Trp53*$^{-/-}$ or *WEA;Trp53*$^{+/+}$ cancer cells differentially affected their phenotype (**Extended Data Fig. 3.4a**). Notably, CM from *WEA;Trp53*$^{-/-}$ and *WEP;Trp53*$^{-/-}$ cells strongly induced *Il1b* mRNA expression in cultured BMDMs as compared to CM from matched *Trp53*$^{+/+}$ controls (**Fig. 3.2e**). In agreement with our mouse data, human monocyte-derived macrophages (hMDMs) cultured with tumor CM of *TP53*$^{-/-}$ MCF-7 human breast cancer cells displayed increased CD206 and CD163 expression compared to hMDMs cultured with CM of p53-proficient MCF-7 cells (**Extended Data Fig. 3.4c**). We also observed increased *IL1B* expression in hMDMs upon exposure to *TP53*$^{-/-}$ MCF-7 cells compared to *TP53*$^{+/+}$ controls (**Extended Data Fig. 3.4d**). These data indicate that cancer cell-intrinsic p53 status dictates the crosstalk between cancer cells and macrophages in a paracrine fashion, resulting in an altered macrophage phenotype and IL-1β production. We also observed elevated levels of *IL1B* mRNA expression in breast tumors of The Cancer Genome Atlas (TCGA) with mutations in *TP53* (*TP53*^{MUT}) compared to *TP53*^{WT} tumors (**Fig. 3.2f**), suggesting similar p53-dependent activation of IL-1β signaling in human breast cancer.

To identify which factor(s) in p53-null tumors mediate TAM activation and subsequent systemic inflammation, we performed RNA sequencing on mammary tumors of 12 different GEMMs (7 p53-null models, 5 p53-proficient models; 145 tumors in total). The p53-deficient tumors differed substantially from p53-proficient tumors in terms of gene expression, regardless of any additional genetic aberrations, demonstrating a dominant effect of p53-loss on the global transcriptome (**Extended Data Fig. 3.5a**). Interestingly, the most significantly changed pathways in p53-deficient tumors pertained to adaptive immune phenotypes (**Fig. 3.3a**). While neutrophil and TAM numbers were altered intratumorally, the composition of CD8$^+$, CD4$^+$ or FOXP3$^+$ T cells did not correlate with p53-status (**Extended Data Fig. 3.5b–g**), suggesting that the distinct transcriptome profiles are not due to a p53-dependent effect on the composition of the adaptive immune landscape.

From the gene ontology analysis, we selected genes encoding secreted factors that could potentially influence TAMs. One of the up-regulated pathways in p53-null tumors included WNT/β-catenin signaling (**Fig. 3.3a**). WNT signaling is linked to IL-1β production in acute arthritis, as well as immune and stromal signaling in cancer[20-23]. Using a WNT/β-catenin signaling gene signature, we found that p53-null GEMM tumors clustered separately from p53-proficient tumors, indicating an association between p53-loss and WNT-related gene expression (**Extended Data Fig. 3.6a, b**). Many WNT-related genes were up-regulated in p53-deficient tumors, including three WNT ligands, *WNT1*, *WNT6* and *WNT7a*, while expression of negative regulators of WNT signaling was decreased (**Fig. 3.3b, Extended Data Fig. 3.6c**). Elevated protein levels of WNT1 and WNT7A were confirmed in a set of independent p53-deficient tumors (**Fig. 3.3c, d**). We also found increased expression of non-phosphorylated β-catenin, indicative of activated WNT signaling (**Fig. 3.3c, d**). In human breast tumors, expression of *WNT1, WNT6* and *WNT7A* was increased upon aberrant expression of *TP53,* compared to *TP53*^{WT} tumors (**Fig. 3.3e**). We then broadened our analysis of TCGA data to other WNT-related genes and discovered a trend towards enrichment of

these genes in *TP53*-mutated tumors (**Extended Data Fig. 3.6d**). Additionally, individual WNT-stimulating genes were upregulated, while WNT-inhibiting genes were downregulated in *TP53*^{MUT} versus *TP53*^{WT} human tumors (**Extended Data Fig. 3.6e**), indicating that WNT signaling is activated upon aberrant expression of *TP53*. Using WEA cell lines, we confirmed that WNT1, WNT6 and WNT7A proteins are increased intracellularly in *WEA;Trp53*$^{-/-}$ cells and secreted, when compared to *WEA;Trp53*$^{+/+}$ cells (**Fig. 3.3f**). Collectively, these data indicate cancer cell-autonomous WNT ligand secretion upon loss of p53.

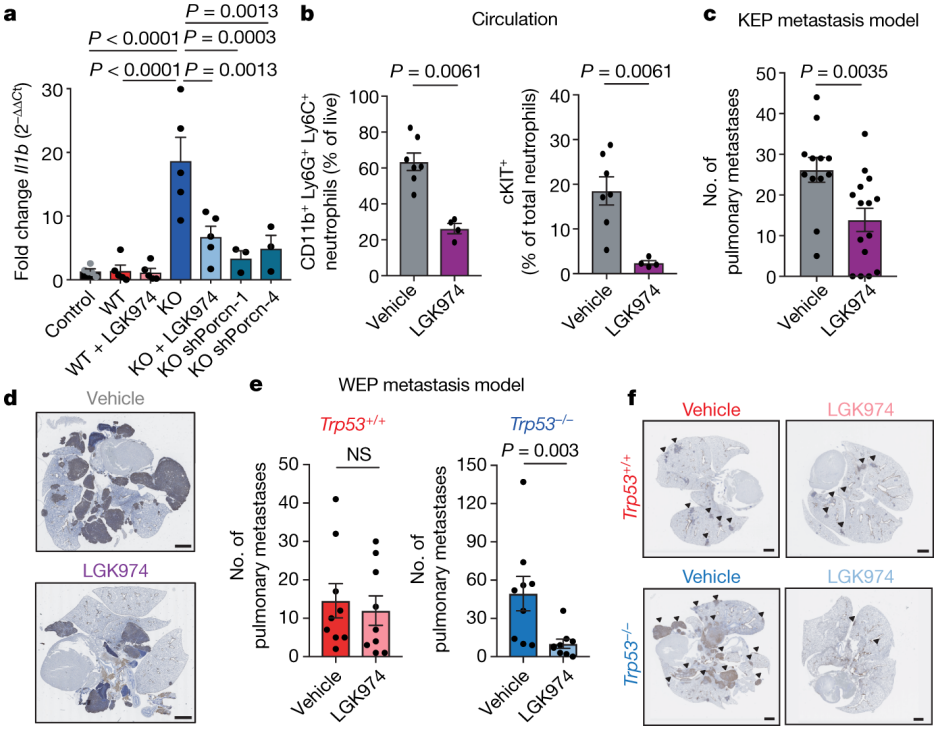

Figure 3.4. WNT-induced systemic inflammation promotes metastasis of p53-null tumors. a. RT-qPCR analysis of bone marrow-derived macrophages (BMDM) after exposure to control medium or conditioned medium from *Wap-cre;Cdh1*$^{F/F}$*;Akt*^{E17K}*;Trp53*$^{+/+}$ (WT), *Wap-cre;Cdh1*$^{F/F}$*;Akt*^{E17K}*;Trp53*$^{-/-}$ (KO) or *Wap-cre;Cdh1*$^{F/F}$*;Akt*^{E17K}*;Trp53*$^{-/-}$ cells transduced with 2 independent shRNAs against *Porcn* (KO shPorcn-1 and KO shPorcn-4). Where indicated, cell lines were pre-treated with 1 μM LGK974 (KO + LGK974) (n=5 biological replicates/group for WT, WT + LGK974, KO and KO + LGK974, n=3 biological replicates for KO shPorcn-1 and KO shPorcn-4). Plots show representative data of 3 separate experiments with 2 technical replicates per biological replicate. **b.** Frequency of total CD11b$^+$Ly6G$^+$Ly6C$^+$ neutrophils and cKIT$^+$ neutrophils in circulation of *K14cre;Cdh1*$^{F/F}$*;Trp53*$^{F/F}$ (KEP) mice after 5 day LGK974 (n=4) or vehicle (n=7) treatment starting at tumor volume 500 mm^3. **c.** Number of pulmonary metastases after KEP tumor-bearing mice were treated with LGK974 (n=15) or vehicle (n=12). KEP tumor fragments were orthotopically transplanted in FVB/N mice and treatment was initiated when tumors were 30 – 40 mm^3 and continued until primary tumor removal. **d.** Representative images of cytokeratin-8 staining of lungs of KEP tumor-bearing mice. Scale bars, 1.9 mm. **e.** Number of pulmonary metastases after orthotopic injection of *Trp53*$^{+/+}$ and *Trp53*$^{-/-}$ *Wap-cre;Cdh1*$^{F/F}$*;Pik3ca*^{E545K} (WEP) cells and treatment with LGK974 or vehicle (n=9/group). Treatment was initiated when tumors were 30 – 40 mm^3 and continued until 1500 mm^3. **f.** Representative images of cytokeratin-8 staining of lungs of WEP tumor-bearing mice, arrows indicate examples of metastatic nodules. Scale bars, 1.4 mm. All data are means ± s.e.m. *P*-values are indicated as determined by two-tailed one-way ANOVA, Tukey's multiple-testing correction (**a**) or two-tailed Mann-Whitney U-test (**b, c, e**), ns: non-significant.

Since deletion of p53 increases WNT ligand expression, we hypothesized that wild-type p53 negatively regulates these genes, either directly or indirectly. To determine whether p53 binds the regulatory regions of *WNT1, WNT6* and/or *WNT7a*, we performed chromatin immunoprecipitation-sequencing (ChIP-seq) in 3 independent WEA and WEP cell lines. p53 binding was observed at the *Cdkn1a* (p21) locus (**Extended Data Fig. 3.7a**), whereas we did not find p53 binding at the *WNT1, WNT6* or *WNT7a* loci (**Extended Data Fig. 3.7b**), suggesting that p53 regulates their expression indirectly. Since p53 has been described to control *WNT1* expression by activating microRNA-34a (miR-34a)[24], we wondered whether this microRNA may be involved in the regulation of *WNT1*, *WNT6* and *WNT7a*. Indeed, we observed p53 chromatin binding at the miR-34a locus in all cell lines (**Extended Data Fig. 3.7c**). Overexpression of miR-34a in *WEA;Trp53*$^{-/-}$ cells resulted in a significant reduction of WNT ligand expression (**Extended Data Fig. 3.7d**). These data suggest that wild-type p53 negatively regulates the expression of *WNT1, WNT6* and *WNT7a* via miR-34a.

We then assessed the role of cancer cell-derived WNT ligands on IL-1β production by macrophages. We treated WEA cells with LGK974 – which inhibits Porcupine (*Porcn*), a WNT-specific acyltransferase that regulates WNT ligand secretion[25] – and added CM to macrophages. LGK974 reduced the *WEA;Trp53*$^{-/-}$ cell-induced *Il1b* expression by macrophages (**Fig. 3.4a**). We also depleted *Porcn* in *WEA;Trp53*$^{-/-}$ cells using short hairpin RNAs (shRNA) and knockdown reduced *Il1b* expression by macrophages, consistent with pharmacological Porcupine inhibition (**Fig. 3.4a**). These data confirm a causal relationship between WNT ligand secretion by p53-deficient cancer cells and IL-1β expression in macrophages.

To identify the receptors involved in the crosstalk between p53-null cancer cells and macrophages, we looked for genes encoding WNT receptors in the GEMM gene expression data. We found that Frizzled receptors, *Fzd7* and *Fzd9,* were up-regulated in the p53-null tumors compared to p53-proficient tumors (**Extended Data Fig. 3.8a**). Similarly, *FZD7* and *FZD9* were increased in expression in *TP53*^{MUT} human breast tumors compared to *TP53*^{WT} tumors (**Extended Data Fig. 3.8b**). We then used small interfering RNAs (siRNA) to knockdown both *Fzd7* and *Fzd9* in BMDMs (**Extended Data Fig. 3.8c**), which prevented *Il1b* induction by *WEA;Trp53*$^{-/-}$ cells (**Extended Data Fig. 3.8d**), demonstrating that that FZD7 and FZD9 are involved in WNT-induced activation of macrophages *in vitro.*

We next assessed whether WNT ligand production by p53-deficient cancer cells drives systemic inflammation. We treated tumor-bearing KEP mice with LGK974 for five consecutive days and this led to a reduction in total neutrophils and cKIT^{+} neutrophils in blood and lungs when compared to vehicle-treated KEP mice (**Fig. 3.4b, Extended Data Fig. 3.9a**). Additionally, IL-17A-producing γδ T cells – the key cell type responding to IL-1β that drive neutrophil accumulation and consequently metastasis[5] – were reduced in the lungs of LGK974-treated KEP mice (**Extended Data Fig. 3.9b**), indicating that γδ T cell activation upstream of pro-metastatic neutrophil accumulation depends on WNT signaling. Similarly, long-term treatment of KEP mice with LGK974 blocked neutrophil expansion over time (**Extended data Fig. 3.9c**). To exclude that the observed reduction in inflammation is a result of targeting non-tumor cells by LGK974, we orthotopically transplanted *WEA;Trp53*$^{-/-}$*;shPorcn* cell lines and matched *WEA;Trp53*$^{-/-}$*;shControl* cells into WT mice. Analysis of size-matched end-stage tumors revealed an incomplete reduction of *Porcn* expression (**Extended Data Fig. 3.9d**). Although we cannot formally exclude the possibility that non-cancer cells contribute to the residual *Porcn* expression, expression levels of *Porcn* in the tumors

correlated with circulating neutrophils, cKIT$^+$ neutrophils and *Il1b* expression (**Extended Data Fig. 3.9e–g**). Moreover, knockdown of *Porcn* prevented splenomegaly (**Extended Data Fig. 3.9h**). Collectively, these data confirm the causal link between WNT secretion triggered by p53-deficient mammary tumors and systemic inflammation.

Since the γδ T cell–neutrophil axis promotes metastasis[4,5] and these cells are regulated by WNT ligands, we hypothesized that LGK974 treatment may present a viable therapeutic strategy to inhibit metastasis of p53-null mammary tumors. To test this, we treated KEP tumor-bearing mice with LGK974 or vehicle, after which we surgically removed the primary tumor and assessed metastatic progression. Strikingly, while Porcupine blockade did not affect primary tumor growth (**Extended Data Fig. 3.9i**), pulmonary metastases were reduced (**Fig. 3.4c, d**). In an independent metastasis model in which we orthotopically transplanted matched *Trp53*$^{+/+}$ and *Trp53*$^{-/-}$ WEP cell lines, we observed that the absence of p53 increases lung metastasis formation (**Fig. 3.4e**, left and right graphs; P=0.0153). We then treated both *WEP;Trp53*$^{+/+}$ and *WEP;Trp53*$^{-/-}$ tumor-bearing mice with LGK974, which failed to influence primary tumor growth (**Extended Data Fig. 3.9j**). However, LGK974 treatment reduced metastasis of *WEP;Trp53*$^{-/-}$ tumors, without affecting metastasis of *WEP;Trp53*$^{+/+}$ tumors (**Fig. 3.4e, f**). These data show that blocking WNT-induced systemic inflammation impedes metastasis formation of p53-null mammary tumors.

In summary, we show that p53 status is an important driver of systemic pro-metastatic inflammation in breast cancer (**Extended Data Fig. 3.9k**) and that targeting WNT signaling may represent a promising therapeutic modality for patients with p53-deficient breast tumors. Together with recent literature on the importance of canonical driver mutations in shaping the local immune composition of primary tumors[26], our findings shed light on the poorly understood inter-patient heterogeneity in the systemic composition and function of immune cells. Mechanistic understanding of the intricate interactions between cancer cell-intrinsic genetic events and the immune landscape provides a basis for the design of personalized immune intervention strategies for cancer patients.

Methods

Mice

All animal experiments were approved by the Animal Ethics Committee of the Netherlands Cancer Institute and performed in accordance with institutional, national and European guidelines for Animal Care and Use. The generation and characterization of the mouse models has been described[27-34] (and unpublished). The following mouse models were used in this study: *Keratin14 (K14)-cre;Cdh1$^{F/F}$;Trp53$^{F/F}$*, *K14cre;Trp53$^{F/F}$*, *K14cre;Brca1$^{F/F}$;Trp53$^{F/F}$*, *Whey Acidic Protein (Wap)-cre;Trp53$^{F/F}$*, *Wap-cre;Brca1$^{F/F}$;Trp53$^{F/F}$*, *Wap-cre;Brca1$^{F/F}$;Trp53$^{F/F}$;Col1a1$^{invCAG\text{-}Met\text{-}IRES\text{-}Luc/+}$* (*Wap-cre;Brca1$^{F/F}$;Trp53$^{F/F}$;Met*), *Wap-cre;Brca1$^{F/F}$;Trp53$^{F/F}$;Col1a1$^{invCAG\text{-}Myc\text{-}IRES\text{-}Luc/+}$* (*Wap-cre;Brca1$^{F/+}$;Trp53$^{F/F}$;Myc*), *Wap-cre;Brca1$^{F/F}$;Trp53$^{F/F}$;Col1a1$^{invCAG\text{-}Myb2\text{-}IRES\text{-}Luc/+}$* (*Wap-cre;Brca1$^{F/F}$;Trp53$^{F/F}$;Myb2*), *Wap-cre;Trp53$^{F/F}$;Col1a1$^{invCAG\text{-}ESR1\text{-}IRES\text{-}Luc/+}$* (*Wap-cre;Trp53$^{F/F}$;HA-ESR1*), *Wap-cre;Cdh1$^{F/F}$;Col1a1$^{invCAG\text{-}AktE17K\text{-}IRES\text{-}Luc/+}$* (*Wap-cre;Cdh1$^{F/F}$;Akt^{E17K}*), *Wap-cre;Cdh1$^{F/F}$;Col1a1$^{invCAG\text{-}Pik3caE545K\text{-}IRES\text{-}Luc/+}$* (*Wap-cre;Cdh1$^{F/F}$;Pik3ca^{E545K}*), *Wap-cre;Cdh1$^{F/+}$;Col1a1$^{invCAG\text{-}Fgfr2ex1\text{-}15\text{-}IRES\text{-}Luc/+}$* (*Wap-cre;Cdh1$^{F/+}$;Fgfr2$^{ex1\text{-}15}$*), *Wap-cre;Cdh1$^{F/F}$;Col1a1$^{invCAG\text{-}Fgfr2ex1\text{-}15\text{-}IRES\text{-}Luc/+}$* (*Wap-cre;Cdh1$^{F/F}$;Fgfr2$^{ex1\text{-}15}$*), *Wap-cre;Cdh1$^{F/F}$;T2/Onc;Rosa26$^{Lox66SBLox71/+}$ (Wap-cre;Cdh1$^{F/F}$;SB*), *Wap-cre;Map3k1$^{F/F}$;Pten$^{F/F}$*, *Mouse mammary tumor virus LTR (MMTV)-NeuT*. All mouse models were on FVB/N background, except *MMTV-NeuT* and *Wap-cre;Cdh1$^{F/F}$;SB*, which were on Balb/c and a mixed genetic (C57BL/6J and FVB/N) background, respectively. Female mice were monitored twice weekly for the onset of spontaneous mammary tumor formation by palpation starting at 6-7 weeks of age. The perpendicular tumor diameters of mammary tumors were measured twice per week using a caliper, and tumor volume was calculated using *vol(mm^3) = 0.5(length x width^2)*. Maximum permitted tumor volumes were 1500 mm^3. Age-matched WT littermates were used as controls. Average systemic total and cKIT$^+$ neutrophil levels in non-tumor-bearing FVB/N and Balb/c mice were similar (data not shown).

For orthotopic transplantation experiments, 1x10^6 cells were injected into the right 4th mammary fat pad of WT FVB/N mice (Janvier Labs). For intervention studies targeting Porcupine, *K14cre;Cdh1$^{F/F}$;Trp53$^{F/F}$* mice were treated daily with LGK974[35] (10 mg/kg, in 10% DMSO/10% Cremophor in PBS) or vehicle (10% DMSO/10% Cremophor in PBS) via oral gavage, starting at matched tumor sizes indicated in the figures. For metastasis experiments, the KEP-based model for spontaneous breast cancer metastasis was used as previously described[36]. Briefly, tumor fragments of *K14cre;Cdh1$^{F/F}$;Trp53$^{F/F}$* mice were orthotopically transplanted into FVB/N mice and surgically removed when tumors reached 500 mm^3 in size. In this model, LGK974 treatment was initiated when tumors were 30 – 40 mm^3 in size and continued until mastectomy, after which mice were monitored for signs of metastatic disease. Disease endpoint was defined as mice showing signs of respiratory distress or palpable metastatic nodules in lymph nodes or other organs reaching 1500 mm^3 in size. For metastasis experiments using the *Wap-cre;Cdh1$^{F/F}$;Pik3ca^{E545K}* model, matched *Trp53$^{+/+}$* and *Trp53$^{-/-}$* tumor-derived cell lines were orthotopically injected in the mammary fat pad of FVB/N mice (1x10^6 cells) and tumors were allowed to grow out until end stage (1500 mm^3). During this time, tumors spontaneously metastasize to the lungs. LGK974 or vehicle treatment was initiated when tumors were 30 – 40 mm^3 and continued until end stage. Orthotopically transplanted *Wap-cre;Cdh1$^{F/F}$;Akt^{E17K}* tumors did not spontaneously metastasize before the primary tumors reached 1500 mm^3, and surgical removal of the primary tumor was hampered by its highly invasive growth. For intervention studies, mice were randomly distributed over the two treatment arms when tumors reached the indicated size. Tumor measurements and

post mortem analyses were performed in a blinded fashion. Mice were kept in individually ventilated cages, and food and water were provided *ad libitum*. The maximal permitted disease endpoints were not exceeded in any of the experiments.

Flow cytometry

Flow cytometry analysis was performed as previously described[5]. Briefly, tissues were collected in ice-cold PBS and blood was collected in tubes containing heparin. Tumors and lungs were mechanically chopped using a McIlwain tissue chopper (Mickle Laboratory Engineering). Tumors were digested for 1 hour (h) at 37°C in 3 mg/mL collagenase type A (Roche) and 25 µg/mL DNase (Sigma) in serum-free DMEM medium. Lungs were digested for 30 minutes (min) at 37°C in 100 µg/mL Liberase TM (Roche). Enzyme reactions were stopped by addition of cold DMEM/8% Fetal Calf Serum (FCS) and suspensions were dispersed through a 70 µm cell strainer. Bone marrow was collected from the tibia and femurs of both hind legs and flushed using RPMI/8% FCS through a 70 µm cell strainer. Single-cell suspensions were treated with NH_4Cl erythrocyte lysis buffer. Before staining, cell suspensions were subjected to Fc receptor blocking (rat anti-mouse CD16/32, BD Biosciences) for 15 min at 4°C, except for bone marrow (to allow assessment of CD16/32 expression). Cells were stained with conjugated antibodies for 30 min at 4°C in the dark in PBS/0.5% BSA. 7AAD (1:20; eBioscience/ThermoFisher) or Fixable Viability Dye eFluor 780 (1:1000; eBioscience/ThermoFisher) was added to exclude dead cells. For intracellular cytokine staining, single-cell suspensions were stimulated in IMDM containing 8% FCS, 100 IU/mL penicillin, 100 mg/mL streptomycin, 0.5% β-mercaptoethanol, 50 ng/ml PMA, 1 mM ionomycin and Golgi-Plug (1:1,000; BD Biosciences) for 3h at 37°C. Surface antigens were stained first, followed by fixation and permeabilization using the Cytofix/Cytoperm kit (BD Biosciences) and staining of intracellular proteins. All antibodies used are listed in **Supplemental Table 3.1**. All experiments were performed using a BD LSR II flow cytometer using Diva software or the Beckman Coulter CyAn ADP flow cytometer using Summit software. Data analyses were performed using FlowJo Software version 9.9.

Cell culture

Mouse cell lines were generated as follows: *Wap-cre;Cdh1$^{F/F}$;Akt^{E17K}* (WEA) and *Wap-cre;Cdh1$^{F/F}$;Pik3ca^{E545K}* (WEP) tumor material was collected in ice-cold PBS and mechanically chopped using a McIlwain tissue chopper (Mickle Laboratory Engineering). Tumors were subsequently digested for 30 min at 37°C in 3 mg/mL Collagenase A, 0.1% trypsin and fungizone in DMEM/2% FCS. Enzyme reactions were stopped by addition of DMEM/2% FCS and suspensions were dispersed through a 40 µm cell strainer. Cells were initially cultured in DMEM containing 10% FCS, 100 IU/mL penicillin, 100 mg/mL streptomycin, Insulin, EGF and Cholera toxin. After establishment, mouse cell lines were cultured in DMEM medium supplemented with 8% FCS, 100 IU/mL penicillin, 100 mg/mL streptomycin and 2 mM L-glutamine. To ensure relatedness to parental GEMM tumors, polyclonal cells were used at low passage number for all experiments. MCF-7 cells (provided by T.N. Schumacher) were cultured in DMEM medium supplemented with 8% FCS, 100 IU/mL penicillin, 100 mg/mL streptomycin and 2 mM L-glutamine. All cell lines were routinely tested for mycoplasma contamination and only mycoplasma-negative cells were used. For *in vitro* culture of bone marrow-derived macrophages (BMDMs), bone marrow was aseptically collected by flushing tibia and femurs from euthanized WT mice with sterile RPMI/8% FCS. Bone marrow cells were

cultured for 7 days in RPMI medium supplemented with 8% FCS, 100 IU/mL penicillin, 100 mg/mL streptomycin and 10 ng/mL recombinant M-CSF (Peprotech). BMDMs were harvested at day 7 and examined for CD11b and F4/80 expression by flow cytometry. Consistent purities of >95% $CD11b^+F4/80^+$ cells were obtained. For *in vitro* culture of human monocyte-derived macrophages (MDMs), human PBMCs (Sanquin, Amsterdam) were enriched by magnetically activated cell sorting (MACS) using CD14 microbeads (Miltenyi Biotec). $CD14^+$ cells were cultured in RPMI medium supplemented with 8% FCS, 100 IU/mL penicillin, 100 mg/mL streptomycin and 10 ng/mL recombinant M-CSF (Peprotech). MDMs were harvested at day 7 and examined for CD11b, CD14 and CD68 expression by flow cytometry. Consistent purities of >95% $CD11b^+CD14^+CD68^+$ cells were obtained. Where indicated, BMDMs and MDMs were exposed to conditioned medium (CM) from tumor cell lines, in presence or absence of LGK974 (1 μM, Selleck Chemicals) for 24 h and harvested for RNA and/or protein isolation. CM was obtained by culturing tumor cells at equal confluency in empty DMEM overnight. Cell growth kinetics *in vitro* were analyzed using the IncuCyte System (Essen BioScience).

RNA isolation and quantitative RT-PCR

RNA was isolated using either Trizol or a Qiagen Rneasy column followed by treatment with DNase I (Invitrogen). RNA quality was confirmed with a 2100 Bioanalyzer from Agilent. RNA was converted to complementary DNA (cDNA) with an AMV reverse transcriptase using Oligo(dT) primers (Invitrogen). cDNA (20 ng per well) was analyzed by SYBR green real-time PCR with 500 nM primers using a LightCycler 480 thermocycler (Roche). β-actin and/or GAPDH were used as reference genes. Primer sequences used for each gene are listed in **Supplemental Table 3.2**. Fold change in expression was calculated using $2^{-(\Delta Ct.x - average[\Delta Ct.control])}$.

Protein isolation and western blotting

Protein lysates of cells and tissue were prepared using RIPA buffer (50 mM Tris-HCl, pH 7.4, 150 mM NaCl, 1% NP40, 0.5% DOC, 0.1% SDS, 2 mM EDTA) complemented with protease and phosphatase inhibitors (Roche) and protein concentration was quantified using the BCA protein assay kit (Pierce). Protein lysate was loaded onto NuPAGE 4–12% Bis-Tris gradient gels (Invitrogen) and transferred onto Trans-Blot® Turbo™ Mini or Midi Nitrocellulose membranes (BioRad) using Trans-Blot Turbo Transfer System (BioRad). Membranes were blocked in 10% Western Blot Blocking Reagent (Roche) or 3% BSA for 1 h at room temperature (RT). Primary antibody incubation was performed overnight at 4°C. Membranes were washed using TBS-T and subjected to secondary fluorochrome-conjugated antibodies for 1 h at RT and protein was detected using the Odyssey CLx imaging system and processed using ImageJ software 1.48v. Antibodies are listed in **Supplemental Table 3.1**.

Immunohistochemistry

Immunohistochemical analyses were performed by the Animal Pathology facility at the Netherlands Cancer Institute. Formalin-fixed tissues were processed, sectioned and stained as described[36]. Briefly, tissues were fixed for 24 h in 10% neutral buffered formalin, embedded in paraffin, sectioned at 4 μm and stained with hematoxylin and eosin (H&E) for histopathological evaluation. H&E slides were digitally processed using the Aperio ScanScope (Aperio, Vista, CA). For immunohistochemical analysis, 5 μm paraffin sections were cut, deparaffinized and stained. Antibodies and antigen retrieval methods are listed

in **Supplemental Table 3.1**. Quantitative analysis of cell abundance was performed by counting cells in five high-power (x40) fields of view (FOV) per tissue by two independent researchers. Samples were visualized with a BX43 upright microscope (Olympus) and images were acquired in bright field using cellSens Entry software (Olympus). To score pulmonary metastasis, single lung sections were stained for cytokeratin-8 and metastatic nodules were counted by two independent researchers. Stained tissue slides were digitally processed using the Aperio ScanScope. Brightness and contrast for representative images were adjusted equally among groups.

Cytokine analyses

Quantification of cytokine and chemokine levels in serum was performed using BD Cytometric Bead Array for CCL2, IL-1β, IL-17A and G-CSF according to manufacturer's instructions and analyzed on a Beckman Coulter CyAn ADP flow cytometer with Summit software. Data analyses were performed using FlowJo Software version 9.9.

CRISPR/Cas9-mediated gene disruption

For knock-out of murine *Trp53*, p53-proficient tumor cell lines were transfected with lentiCRISPR v2 (provided by F. Zhang (Addgene plasmid #52961) [37]) containing sgRNA targeting exon 4 (sgRNA1: 5'- TCCGAGTGTCAGGAGCTCCT-3' and sgRNA2: 5'-AGTGAAGCCCTCCGAGTGTC-3'). For knock-out of human *TP53*, MCF-7 tumor cell lines were transfected with lentiCRISPRv2 containing sgRNA targeting either exon 4 (sgRNA1: 5'-CCATTGTTCAATATCGTCCG-3') or exon 2 (sgRNA2: 5'-TCGACGCTAGGATCTGACTG-3'). Cloning of sgRNAs in lentiCRISPR was performed as described[37] and sgRNA sequences were designed using the online CRISPR Design tool (http://crispr.mit.edu), of which the two highest scoring sequences were chosen. All vectors were validated by Sanger sequencing. After selection of transfected cells, polyclonal cell lines were used for all subsequent experiments. To determine knock-out efficiency, genomic DNA from cell lines was isolated using Viagen DirectPCR Lysis reagent (Cell) supplemented with 200 µg/mL proteinase K after transfection and puromycin selection. Murine *Trp53* target region was amplified using PCR with the following primers: FW 5'-GGGGACTGCAGGGTCTCAGA-3' and RV 5'-CCACGTCCCCTGGAGAGATG-3'. Human *TP53* target region was amplified using PCR with the following primers: FW1 5'-CAGACTGCCTTCCGGGTCAC-3' for sgRNA1, FW2 5'-TGGGAAGGTTGGAAGTCCCTC-3' for sgRNA2, and RV 5'-CACTGACAGGAAGCCAAAGGG-3'. PCR products were run on 1% agarose gel, purified using the Illustra GFX™ PCR DNA and Gel Band Purification Kit (Sigma), and subjected to Sanger sequencing using their respective FW primers. Genome editing efficiency was quantified using the Tracking of Indels by Decomposition (TIDE) algorithm as described (http://tide.nki.nl)[38].

shRNA-* and *siRNA-mediated knock-down of genes

Vectors for shRNAs were collected from the TRC library. To allow stable expression of shRNAs, HEK293T cells (provided by T.N. Schumacher) were transfected with the pLKO.1 lentiviral vector encoding shRNAs, pPAX packaging vector and VSV-G envelope vector. Five independent shRNA clones were used for each experiment. Virus was harvested at day 4 and 5 and viral titers were determined using the Abm qPCR lentivirus titration kit (LV900). Cells lines were subsequently transduced and selected using puromycin. Knock-

down efficiency was determined by RT-qPCR as compared to non-targeting controls. The shRNA clone used for *Porcupine* knock-down in all experiments after assessment of knock-down efficiency contained following hairpin sequence: 5'-CAACTTTCTATGCCTGTCAAT-3' (shPorcn-1) or 5'-CCCATGTCTTATTGGTTAAAT-3' (shPorcn-4). For *in vivo* experiments, shPorcn-4 was used. To silence *Fzd* receptors, BMDMs were transfected with the following siRNA pools (control siRNA (sc-37007), *Fzd7* (sc-39991), and *Fzd9* (sc-39995), Santa Cruz Biotechnology), according to manufacturer's instructions. Briefly, BMDMs were differentiated as described above, and 24 h before exposure to tumor CM and BMDMs were suspended in transfection medium and incubated with indicated siRNA pools. After 6 h at 37°C, 2X RPMI medium was added (RPMI, 20% serum, 200 IU/mL penicillin, 200 mg/mL streptomycin and 20 ng/mL recombinant M-CSF) and BMDMs were further cultured overnight. After 24 h, the medium was replaced by tumor CM for 24 h, after which gene expression was assessed.

Chromatin immunoprecipitation (ChIP)-sequencing

ChiP-seq was performed as previously described[39]. Briefly, cell lines from *Wap-cre;Cdh1$^{F/F}$;Akt^{E17K}* and *Wap-cre;Cdh1$^{F/F}$;Pik3ca^{E545K}* tumors (3 cell lines from 3 independent mouse tumors per genotype) were fixed in 1% formaldehyde, crosslinked and processed for sonication. 5 µg of p53 antibody (**Supplemental Table 3.1**) and 50 µL of Protein G magnetic beads (Invitrogen) were used for each ChIP. Eluted DNA was sequenced using the Illumina Hiseq 2500 analyzer (using 65 bp reads) and aligned to the *Mus musculus* mm10 reference genome. Peak calling over input control was performed using and MACS 2.0 peak caller. Data was visualized using Easeq[40].

Overexpression of miR-34a

The MSCV-miR-34a retroviral vector (provided by Lin He (Addgene plasmid #63932)[41]) was transfected in HEK293T cells, together with pGag-Pol and VSV-G vectors to generate retrovirus. Mouse cancer cell lines were exposed to viral supernatant and assessed for expression of WNT target genes after puromycin selection.

RNA sequencing and analysis

Total RNA was extracted from tumors using TRIzol reagent (Ambion Life Technologies) according to the manufacturer's instructions. Samples were equimolar pooled and were single-end sequenced for 51 or 65 base pairs on the Illumina Hiseq2000/Hiseq2500 Machine. The reads were aligned against the mouse transcriptome (mm10) using Tophat2 (Tophat version 2.1.0 / Bowtie version 1.0.0) that allows for exon-exon junctions[42,43]. Tophat was guided using a reference genome as well as a reference transcriptome. The reference transcriptome was created using a gene transfer file (GTF) that was downloaded from Ensembl (version 77). Gene counts were generated using a custom script, that functions identically to HTSeq-count[44]. Only reads that mapped uniquely to the transcriptome were used for gene expression quantification. While some of the libraries were generated with strand-specific protocols, all samples have been aligned without taking strandedness into account. Next, differential expression analysis was performed using the R package edgeR[45] in combination with the voom[46] method, using raw read counts as input. Library size normalization was performed during differential expression analysis within the voom function. Genes with *P*-values 0.05 were labelled as differentially expressed. Genes were further filtered for display by requiring them to be protein coding and to have an absolute

$\log_2$ fold change 3 and a *P*-value 0.01. The selected genes were shown in a heatmap of readcounts that were normalized to 10 million reads per sample.

For Hallmark pathway analysis of murine transcriptomes, raw read counts were normalised by trimmed means of M-values computed using the function calcNormFactors (edgeR version 3.20.5 [45]), from which CPM-normalized gene expression values were computed for plotting purposes using the same R-package. CPM-values were subsequently transformed as $f(x) = \log_2(x + 1)$. Ensembl77 murine gene identifiers were then converted to homologous human gene identifiers using the biomaRt-R package (server oct2016.archive.ensembl.org). Gene expression heatmaps for hallmark human gene sets obtained from MsigDB[47] were generated using the *aheatmap*-function provided by the NMF R-package (version 0.20.6). Heatmap columns (containing samples) were ordered according to average linkage (UPGMA) hierarchical sample-clustering based on Pearson correlation-distances between the expression values of displayed genes. Heatmap rows (containing genes) were ordered according to gene expression fold difference between *Trp53*$^{-/-}$ and *Trp53*$^{+/+}$ samples. The R language for statistical computing was used (version 3.4.2) for gene expression normalisation and heatmap generation. Pathway enrichment analysis of *Trp53*$^{-/-}$ and *Trp53*$^{+/+}$ tumors was performed using Ingenuity Pathway Analysis software (QIAGEN), analysing differentially expressed genes with *P* 0.05.

The Cancer Genome Atlas (TCGA) analysis

To obtain a comprehensive view on the cellular processes affected by p53-deficiency in human breast cancer, we performed a gene set enrichment analyses (GSEA) using a 50 hallmark gene sets (Liberzon)[47] on the TCGA breast cancer (BRCA) cohort. First, we classified p53-deficiency based on mutational status. DNA sequencing variant calls (MAF-file) for the BRCA cohort were downloaded from the 2015-08-21 release of the Broad TCGA genome data analysis centre standard run (http://gdac.broadinstitute.org/runs/stddata). We utilized two classifications for p53-deficiency: in the first classification (labelled 'any *TP53* mutation'), patients with any kind of *TP53* mutation were classified as p53-deficient. In the second classification (labelled 'IARC *TP53* database'), only patients with a dominant negative *TP53* mutation as annotated using the IARC *TP53* mutation database[48] (release 18, matched on protein effect of the mutation) were labelled as p53-deficient, as well as patients with gain-of-stop, stop-lost or frameshifting mutations (*n*=161). One sample had a trans-activating mutation and was excluded from the analysis. The remaining samples were labelled as p53-proficient (*n*=793).

Next, TCGA RNA sequencing data were downloaded from the Broad TCGA genome data analysis centre 2015-11-01 release of the standard runs. We ran a gene set enrichment analysis (GSEA) on the 50 Hallmark gene set using the flexgsea-r R package (https://github.com/NKI-CCB/flexgsea-r) on the read counts normalized with limma voom with the span parameter set to 0.5 [46]. Within each permutation of the sample labels, genes were ranked for association with p53-proficiency using the moderated *t*-statistic from the limma empirical Bayes function (ebayes() ran on the result of lmFit()). Reported FDR-values were obtained from the flexgsea-r output.

Single gene associations with *TP53* status in human breast tumors of the TCGA BRCA cohort and correlation coefficients between WNT-related genes and *TP53* status (MUT vs WT) were analysed using R2 Genomics Analysis and Visualization Platform (http://r2.amc.nl/) and visualized using GraphPad Prism version 7.

Statistics and reproducibility

Data analyses were performed using GraphPad Prism (version 7). The statistical tests used are described in figure legends. All tests were performed two-tailed. *P*-values < 0.05 were considered statistically significant. All western blot and RT-qPCR analyses were independently repeated more than twice. Sample sizes were based on previous experiments[5,17,36] or determined using G*Power software (version 3.1). To exclude bias towards one particular GEMM in the analyses for Figure 3.1, we have performed the same analyses on the average of the neutrophil levels and serum cytokine values per model. This demonstrated the same correlations between the assessed values and p53 status of the tumor, thus excluding bias towards one or several particular models. Principal component analysis was performed using the prcomp-function in R (version 3.4.2), both centering and scaling the input data before applying dimensionality reduction.

Reporting summary

Further information on research design is available in the Nature Research Reporting Summary linked to this paper.

Data availability statement

The RNA sequencing data have been deposited in the Gene Expression Omnibus (GEO, NCBI) repository under accession number GSE112665. All other data are found in the source data, supplemental information or available from the authors on reasonable request.

Acknowledgements

Research in the De Visser laboratory is funded by a European Research Council Consolidator award (ERC InflaMet 615300), the Netherlands Organization for Scientific Research (NWO-VICI 91819616), Oncode Institute, the Dutch Cancer Society (KWF10083; KWF10623) and the Beug Foundation for Metastasis Research. K.E.d.V. is an EMBO Young Investigator. We would like to thank members of the De Visser and Jonkers labs and R. Mezzadra for fruitful discussion during the preparation of the manuscript. We thank O. van Tellingen, the Mouse Clinic for Cancer and Aging (MCCA) intervention Unit, flow cytometry facility, mouse transgenic facility, genomics core facility, animal laboratory facility and animal pathology facility of the Netherlands Cancer Institute for technical assistance.

Author contributions

M.D.W., S.B.C., J.J. and K.E.d.V. conceived the ideas and designed the experiments. M.D.W., S.B.C., D.E.M.D. and M.H.v.M. performed the animal experiments, flow cytometry, RT-qPCR, serum analyses, western blot, immunohistochemistry and other experiments and analysed the data. C.H., K.V., A.P.D., E.S. and R.d.K-G. provided technical support and performed animal experiments. M.H.v.M., L.H., S.M.K. and J.J. generated mouse models. M.D.W. and R.d.K-G. performed mouse intervention experiments. I.v.d.H. generated the GEMM-derived cell lines. S.P., M.D.W. and W.Z. performed and analysed the ChIP-seq experiments. M.S., I.d.R., M.D.W., L.F.A.W. and T.N.S. performed the bioinformatics analyses on mouse and human RNA-sequencing datasets. M.D.W., S.B.C. and K.E.d.V. wrote the paper and prepared the figures, with input from all authors.

Competing interests

M.D.W., S.B.C., D.E.M.D., M.H.v.M., M.S., I.d.R., L.H., S.M.K., S.P., C-S.H. K.V., A.P.D., R.d.K-G., E.S. I.v.d.H., W.Z. and J.J. report no competing interests. L.F.A.W. reports research funding from Genmab. T.N.S. is a consultant for Adaptive Biotechnologies, AIMM Therapeutics, Allogene Therapeutics, Amgen, Merus, Neon Therapeutics, Scenic Biotech, Third Rock Ventures, reports research support from Merck, Bristol-Myers Squibb, Merck KGaA, and is stockholder in AIMM Therapeutics, Allogene Therapeutics, Merus, Neogene Therapeutics, Neon Therapeutics, Scenic Biotech, all outside the scope of this work. K.E.d.V. reports research funding from Roche and is consultant for Third Rock Ventures, outside the scope of this work.

Extended Data

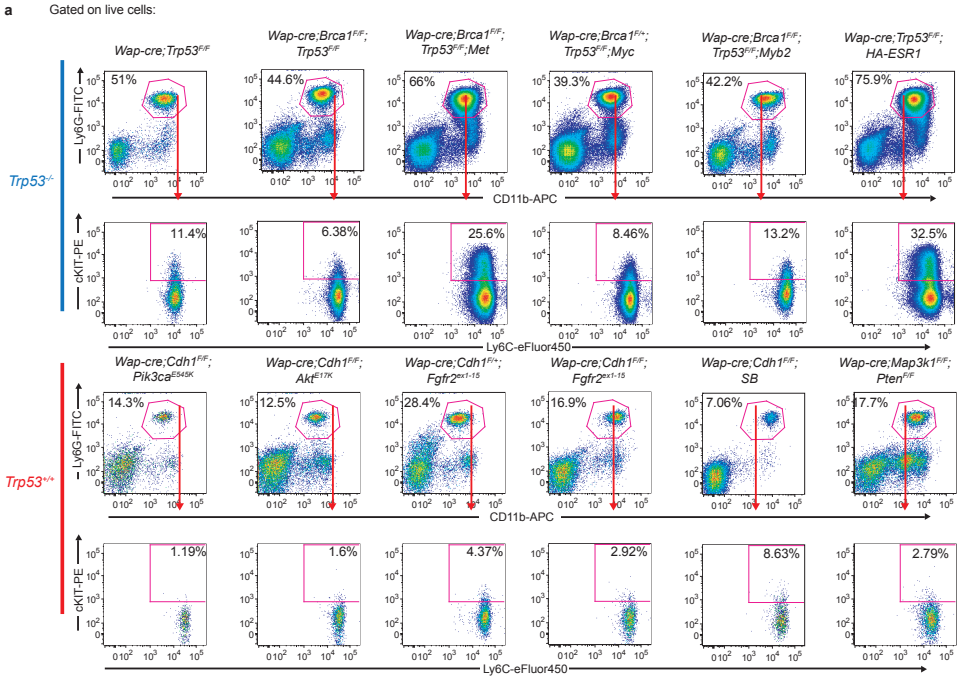

Extended Data Figure 3.1. Neutrophil expansion in p53-deficient tumor-bearing GEMMs. a. Representative plots of flow cytometry analysis on blood of end-stage (cumulative tumor size 1500 mm^3) mammary tumor-bearing mice. Neutrophils were defined as $CD11b^+Ly6G^+Ly6C^+$. cKIT expression on gated total neutrophils in blood is shown (gating was based on blood of WT mice). Quantification and statistical analysis of these data is found in Fig. 1a, b.

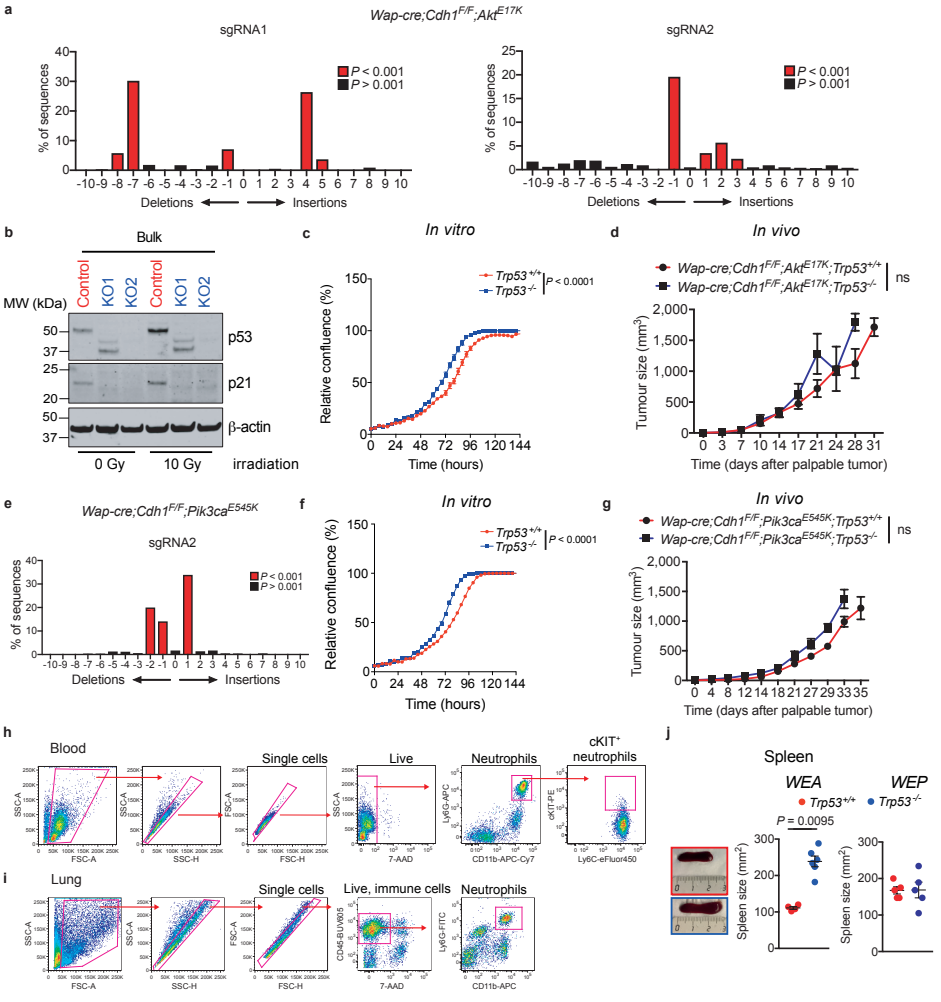
a
Wap-cre;Cdh1F/F;AktE17K
sgRNA1
sgRNA2
% of sequences
P < 0.001
P > 0.001
Deletions
Insertions
b
Bulk
Control
KO1
KO2
MW (kDa)
p53
p21
β-actin
0 Gy
10 Gy
irradiation
c
In vitro
Trp53+/+
Trp53-/-
P < 0.0001
Relative confluence (%)
Time (hours)
d
In vivo
Wap-cre;Cdh1F/F;AktE17K;Trp53+/+
Wap-cre;Cdh1F/F;AktE17K;Trp53-/-
ns
Tumour size (mm3)
Time (days after palpable tumor)
e
Wap-cre;Cdh1F/F;Pik3caE545K
sgRNA2
f
In vitro
g
In vivo
Wap-cre;Cdh1F/F;Pik3caE545K;Trp53+/+
Wap-cre;Cdh1F/F;Pik3caE545K;Trp53-/-
h
Blood
Single cells
Live
Neutrophils
cKIT+ neutrophils
i
Lung
Single cells
Live, immune cells
Neutrophils
j
Spleen
WEA
WEP
Trp53+/+
Trp53-/-
P = 0.0095
Spleen size (mm2)

Extended Data Figure 3.2. CRISPR/Cas9-mediated gene disruption of *Trp53* in *Wap-cre;Cdh1$^{F/F}$;Akt^{E17K}* and *Wap-cre;Cdh1$^{F/F}$;Pik3ca^{E545K}* cancer cell lines. a. Insertion and deletion (indel) spectrum of bulk *Wap-cre;Cdh1$^{F/F}$;Akt^{E17K}* (WEA) cancer cell lines after transfection with 2 individual sgRNAs against *Trp53* and puromycin selection, as determined by the TIDE algorithm and compared to the sequence of target region of control cells. The *P*-value associated with the estimated abundance of each indel is calculated by a two-tailed t-test of the variance–covariance matrix of the standard errors. **b.** Western blot analysis showing p53 levels of control and p53-knockout (KO) WEA cell lines. Inactivation of the p53 pathway is shown by loss of p21 staining after 10 Gy irradiation. KO1 (sgRNA1) resulted in a truncated p53 protein and KO2 (sgRNA2) shows absence of p53 protein. For all subsequent experiments, KO2 was used. Representative of two independent experiments. For uncropped images, see Supplemental Fig. 1 (online). **c.** *In vitro* growth kinetics of WEA control and p53-KO cells, as determined by IncuCyte (*n*=7 technical replicates/group). **d.** *In vivo* growth kinetics of orthotopically transplanted *WEA;Trp53$^{+/+}$* (*n*=4 mice) and *WEA;Trp53$^{-/-}$* (*n*=6) cancer cell lines, with t = 0 being the first day tumors were palpable. **e.** Indel spectrum of bulk *Wap-cre;Cdh1$^{F/F}$;Pik3ca^{E545K}* (WEP) cancer cell lines after transfection with sgRNA2 against *Trp53* and puromycin selection, as determined by the TIDE algorithm. **f.** *In vitro* growth kinetics of *WEP* control and p53-KO cells, as determined by IncuCyte (*n*=7 technical replicates/group). **g.** *In vivo* growth kinetics of orthotopically transplanted *WEP;Trp53$^{+/+}$* (*n*=5) and *WEP;Trp53$^{-/-}$* (*n*=5) cell lines, with t=0 being the first day tumors were palpable. **h.** Gating strategy to identify circulating neutrophils and their cKIT expression. **i.** Gating strategy to identify neutrophils in the lung. **j.** Representative images of spleens from mice bearing *WEA;Trp53$^{+/+}$* and *WEA;Trp53$^{-/-}$* tumors and quantification of spleen area (length x width) at end-stage (tumor volume 1500 mm^3) of mice bearing p53-proficient (*n*=4) and p53-deficient WEA (*n*=6) and WEP tumors (*n*=5/group). All data are means ± s.e.m. *P*-values are indicated as determined by Area Under the Curve followed by two-tailed Welch's t-test (**c, d, f , g**) or two-tailed Mann-Whitney U-test (**j**), ns: not significant.

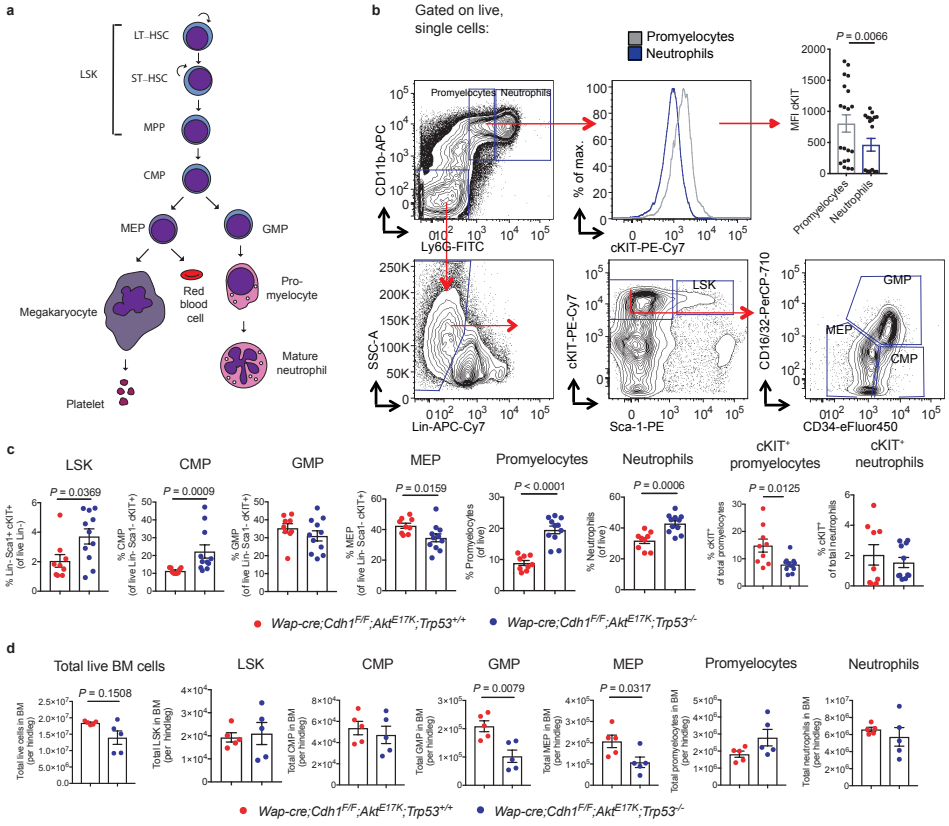

Extended Data Figure 3.3. Hematopoiesis in p53-null tumor-bearing mice is skewed towards the development of neutrophils. a. Schematic representation of neutrophil development in the bone marrow. **b.** Gating strategy of neutrophil progenitor populations in the bone marrow. Dot plot indicates the cKIT expression levels (median fluorescence intensity [MFI]) in promyelocytes compared to mature neutrophils (n=20 mice). **c.** Frequency of bone marrow progenitor populations in mice bearing end-stage *Wap-cre;Cdh1$^{F/F}$;Akt^{E17K};Trp53$^{+/+}$* (n=9) and *Wap-cre;Cdh1$^{F/F}$;Akt^{E17K};Trp53$^{-/-}$* (n=11) tumors, as determined by flow cytometry. **d.** Total live cells and total live progenitor population numbers per hindleg of mice bearing *WEA;Trp53$^{+/+}$* and *WEA;Trp53$^{-/-}$* tumors (n=5/group). All data are ± s.e.m. P-values are indicated as determined by two-tailed Mann-Whitney U-test. Abbreviations: LSK (Lin$^-$Sca1$^+$cKIT$^+$, which contain the LT-HSC (long-term hematopoietic stem cells), ST-HSC (short-term hematopoietic stem cells) and MPP (multipotent progenitors)), CMP (common myeloid progenitors), GMP (granulocytic and monocytic progenitors), MEP (megakaryocyte and erythrocyte progenitors).

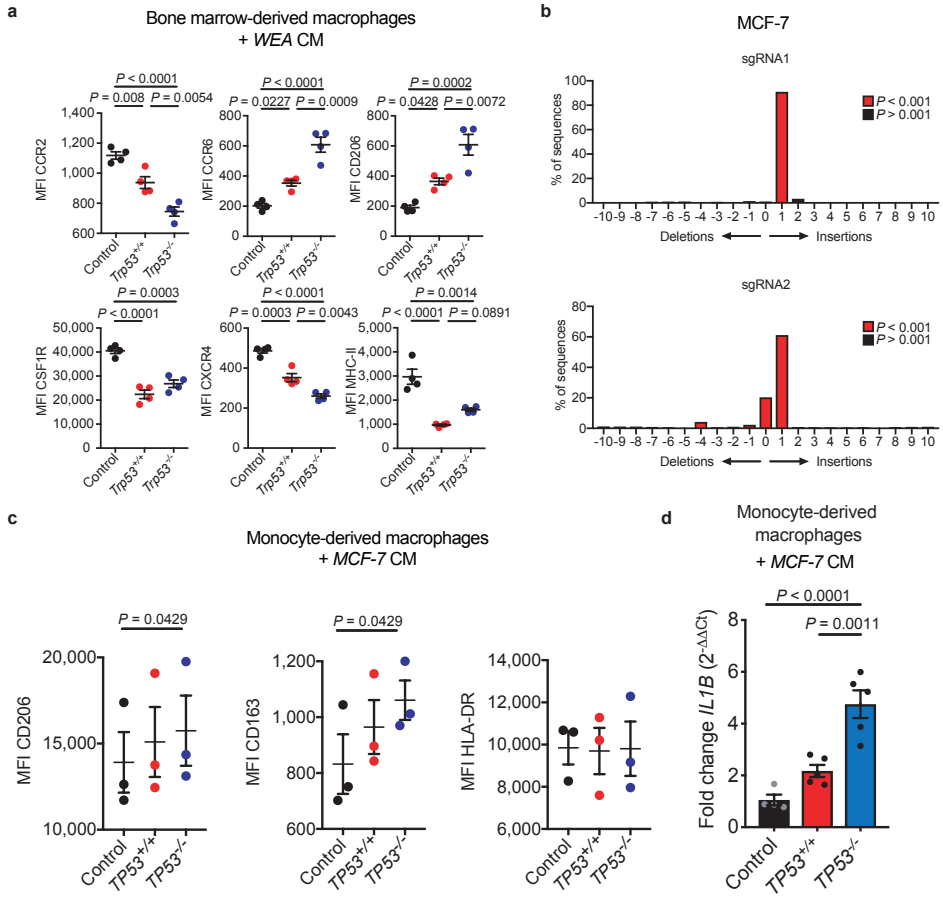

Extended Data Figure 3.4. Macrophages are differentially activated by *Trp53*$^{-/-}$ mouse and human breast cancer cell lines. a. Expression (median fluorescence intensity [MFI]) of CCR2, CCR6, CD206, CSF-1R, CXCR4 and MHC-II on live CD11b^{+}F4/80^{+} bone marrow-derived macrophages after exposure to control medium or conditioned medium (CM) of *Wap-cre;Cdh1*$^{F/F}$*;Akt*^{E17K}*;Trp53*$^{+/+}$ or *Wap-cre;Cdh1*$^{F/F}$*;Akt*^{E17K}*;Trp53*$^{-/-}$ cell lines, as determined by flow cytometry (n=4 biological replicates/group). **b.** TIDE analysis of bulk MCF-7 cells after transfection with *TP53*-targeting sgRNAs and puromycin selection. For subsequent experiments, sgRNA1 was used. **c.** Expression (MFI) of CD206, CD163 and HLA-DR on human CD11b^{+}CD14^{+}CD68^{+} monocyte-derived macrophages (MDMs) after exposure to CM of *MCF-7;TP53*$^{+/+}$ or *MCF-7;TP53*$^{-/-}$ (sgRNA1) cancer cells (n=3 biological replicates/group). **d.** RT-qPCR analysis showing *IL1B* expression in human CD11b^{+}CD14^{+}CD68^{+} MDMs after exposure to control medium (n=4 biological replicates) CM of *MCF-7-TP53*$^{+/+}$ or *MCF-7-TP53*$^{-/-}$cancer cells (n=5 biological replicates/group). Data are normalized to normal medium control. Plots shows representative data of 3 separate experiments and average with 2 technical replicates. All data are means ± s.e.m. *P*-values are indicated as determined by two-tailed one-way ANOVA, Tukey's multiple-testing correction.

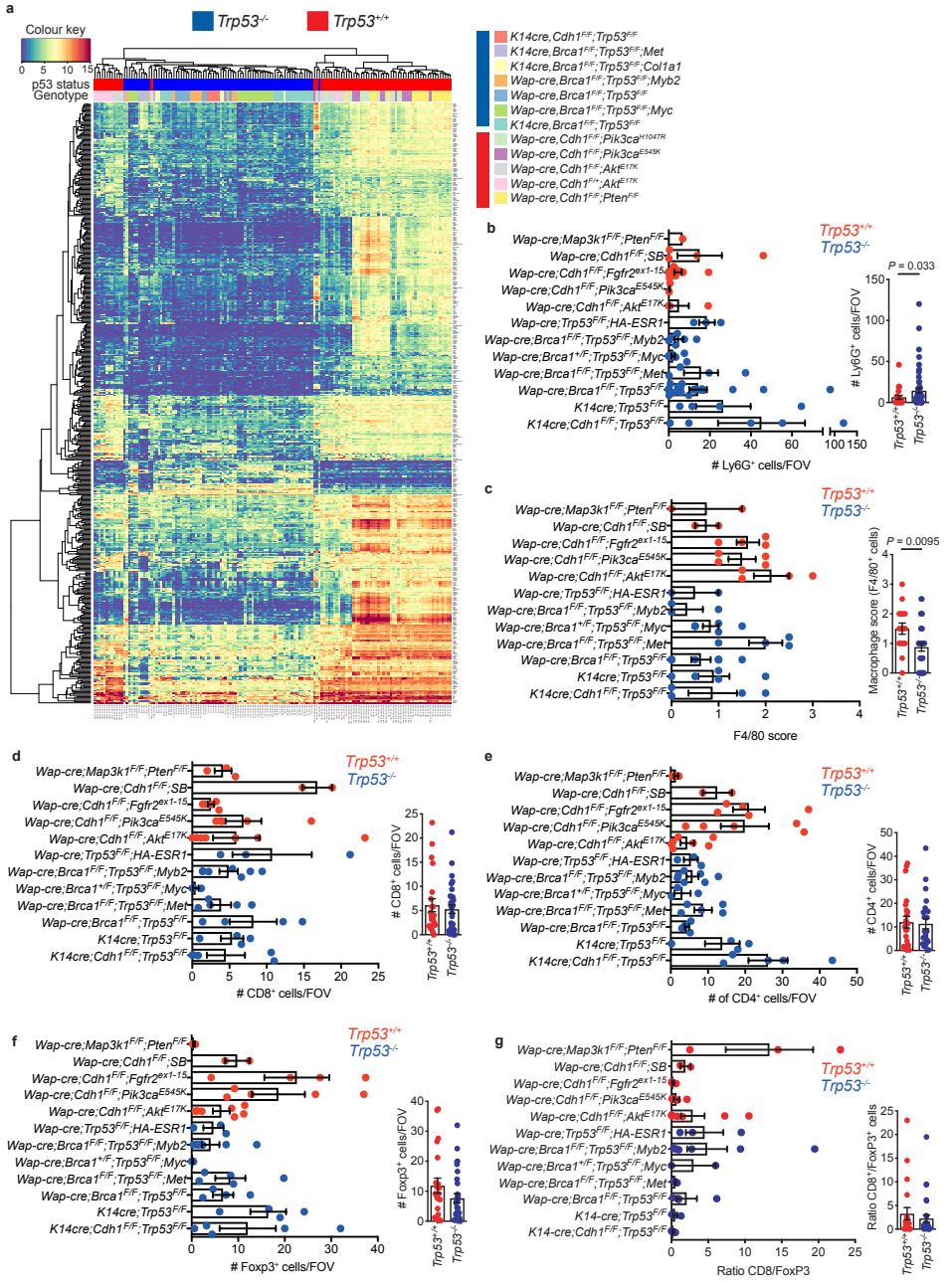
a
Trp53-/-
Trp53+/+
Colour key
0 5 10 15
p53 status
Genotype
K14cre,Cdh1F/F;Trp53F/F
K14cre,Brca1F/F;Trp53F/F;Met
K14cre,Brca1F/F;Trp53F/F;Col1a1
Wap-cre,Brca1F/F;Trp53F/F;Myb2
Wap-cre,Brca1F/F;Trp53F/F
Wap-cre,Brca1F/F;Trp53F/F;Myc
K14cre,Brca1F/F;Trp53F/F
Wap-cre,Cdh1F/F;Pik3caH1047R
Wap-cre,Cdh1F/F;Pik3caE545K
Wap-cre,Cdh1F/F;AktE17K
Wap-cre,Cdh1F/+;AktE17K
Wap-cre,Cdh1F/F;PtenF/F
b
Trp53+/+
Trp53-/-
Wap-cre;Map3k1F/F;PtenF/F
Wap-cre;Cdh1F/F;SB
Wap-cre;Cdh1F/F;Fgfr2ex1-15
Wap-cre;Cdh1F/F;Pik3caE545K
Wap-cre;Cdh1F/F;AktE17K
Wap-cre;Trp53F/F;HA-ESR1
Wap-cre;Brca1F/F;Trp53F/F;Myb2
Wap-cre;Brca1+/F;Trp53F/F;Myc
Wap-cre;Brca1F/F;Trp53F/F;Met
Wap-cre;Brca1F/F;Trp53F/F
K14cre;Trp53F/F
K14cre;Cdh1F/F;Trp53F/F
0 20 40 60 100 150
# Ly6G+ cells/FOV
P = 0.033
150 100 50 0
Ly6G+ cells/FOV
Trp53+/+
Trp53-/-
c
Trp53+/+
Trp53-/-
Wap-cre;Map3k1F/F;PtenF/F
Wap-cre;Cdh1F/F;SB
Wap-cre;Cdh1F/F;Fgfr2ex1-15
Wap-cre;Cdh1F/F;Pik3caE545K
Wap-cre;Cdh1F/F;AktE17K
Wap-cre;Trp53F/F;HA-ESR1
Wap-cre;Brca1F/F;Trp53F/F;Myb2
Wap-cre;Brca1+/F;Trp53F/F;Myc
Wap-cre;Brca1F/F;Trp53F/F;Met
Wap-cre;Brca1F/F;Trp53F/F
K14cre;Trp53F/F
K14cre;Cdh1F/F;Trp53F/F
0 1 2 3 4
F4/80 score
P = 0.0095
4 3 2 1 0
Macrophage score (F4/80+ cells)
Trp53+/+
Trp53-/-
d
Trp53+/+
Trp53-/-
Wap-cre;Map3k1F/F;PtenF/F
Wap-cre;Cdh1F/F;SB
Wap-cre;Cdh1F/F;Fgfr2ex1-15
Wap-cre;Cdh1F/F;Pik3caE545K
Wap-cre;Cdh1F/F;AktE17K
Wap-cre;Trp53F/F;HA-ESR1
Wap-cre;Brca1F/F;Trp53F/F;Myb2
Wap-cre;Brca1+/F;Trp53F/F;Myc
Wap-cre;Brca1F/F;Trp53F/F;Met
Wap-cre;Brca1F/F;Trp53F/F
K14cre;Trp53F/F
K14cre;Cdh1F/F;Trp53F/F
0 5 10 15 20
CD8+ cells/FOV
25 20 15 10 5 0
CD8+ cells/FOV
Trp53+/+
Trp53-/-
e
Trp53+/+
Trp53-/-
Wap-cre;Map3k1F/F;PtenF/F
Wap-cre;Cdh1F/F;SB
Wap-cre;Cdh1F/F;Fgfr2ex1-15
Wap-cre;Cdh1F/F;Pik3caE545K
Wap-cre;Cdh1F/F;AktE17K
Wap-cre;Trp53F/F;HA-ESR1
Wap-cre;Brca1F/F;Trp53F/F;Myb2
Wap-cre;Brca1+/F;Trp53F/F;Myc
Wap-cre;Brca1F/F;Trp53F/F;Met
Wap-cre;Brca1F/F;Trp53F/F
K14cre;Trp53F/F
K14cre;Cdh1F/F;Trp53F/F
0 10 20 30 40 50
# of CD4+ cells/FOV
50 40 30 20 10 0
CD4+ cells/FOV
Trp53+/+
Trp53-/-
f
Trp53+/+
Trp53-/-
Wap-cre;Map3k1F/F;PtenF/F
Wap-cre;Cdh1F/F;SB
Wap-cre;Cdh1F/F;Fgfr2ex1-15
Wap-cre;Cdh1F/F;Pik3caE545K
Wap-cre;Cdh1F/F;AktE17K
Wap-cre;Trp53F/F;HA-ESR1
Wap-cre;Brca1F/F;Trp53F/F;Myb2
Wap-cre;Brca1+/F;Trp53F/F;Myc
Wap-cre;Brca1F/F;Trp53F/F;Met
Wap-cre;Brca1F/F;Trp53F/F
K14cre;Trp53F/F
K14cre;Cdh1F/F;Trp53F/F
0 10 20 30 40
Foxp3+ cells/FOV
40 30 20 10 0
Foxp3+ cells/FOV
Trp53+/+
Trp53-/-
g
Trp53+/+
Trp53-/-
Wap-cre;Map3k1F/F;PtenF/F
Wap-cre;Cdh1F/F;SB
Wap-cre;Cdh1F/F;Fgfr2ex1-15
Wap-cre;Cdh1F/F;Pik3caE545K
Wap-cre;Cdh1F/F;AktE17K
Wap-cre;Trp53F/F;HA-ESR1
Wap-cre;Brca1F/F;Trp53F/F;Myb2
Wap-cre;Brca1+/F;Trp53F/F;Myc
Wap-cre;Brca1F/F;Trp53F/F;Met
Wap-cre;Brca1F/F;Trp53F/F
K14-cre;Trp53F/F
K14-cre;Cdh1F/F;Trp53F/F
0 5 10 15 20 25
Ratio CD8/FoxP3
25 20 15 10 5 0
Ratio CD8+/FoxP3+ cells
Trp53+/+
Trp53-/-

Extended Data Figure 3.5. Transcriptome profile and composition of the local tumor immune landscape in breast cancer GEMMs. a. Unsupervised clustering of top 200 most differentially expressed genes ($P < 0.01$, LFC > 3 or < –3) in mammary GEMM tumors as determined by RNA sequencing (n=145 tumors). Red bars indicate *Trp53*$^{+/+}$ tumors, blue bars indicate *Trp53*$^{-/-}$ tumors. Full tumor genotype is displayed in legend and shown by indicated colors. **b.** Number of Ly6G^{+} neutrophils in the tumor (n=1, 4, 10, 2, 4, 3, 6, 13, 4, 22, 4 and 5 mice, top to bottom). **c.** Macrophage score as indicative of F4/80^{+} macrophage abundance in the tumor (n=2, 2, 4, 4, 4, 2, 3, 5, 4, 9, 5 and 4 mice, top to bottom). **d.** Number of CD8^{+} cytotoxic T cells in the tumor (n=3, 2, 5, 5, 7, 3, 7, 3, 5, 4, 4 and 5 mice, top to bottom). **e.** Number of CD4^{+} T cells in the tumor (n=3, 2, 5, 5, 7, 3, 7, 3, 5, 4, 4 and 5 mice, top to bottom). **f.** Number of Foxp3^{+} regulatory T cells in the tumor (n=3, 2, 5, 5, 7, 3, 7, 3, 5, 4, 4 and 5 mice, top to bottom). **g.** Ratio of CD8/Foxp3 cells in the tumor (n=3, 2, 5, 5, 7, 3, 7, 2, 5, 4, 4 and 5 mice, top to bottom). All data are means of 5 microscopic fields of view (FOV) per mouse as determined by IHC. Inserts show data combined according to p53 status of the tumor. Each symbol represents an individual mouse. All data are means ± s.e.m. P-values are indicated as determined by two-tailed one-way ANOVA, FDR multiple-testing correction (**a**) or two-tailed Mann-Whitney U-test (**b – g**).

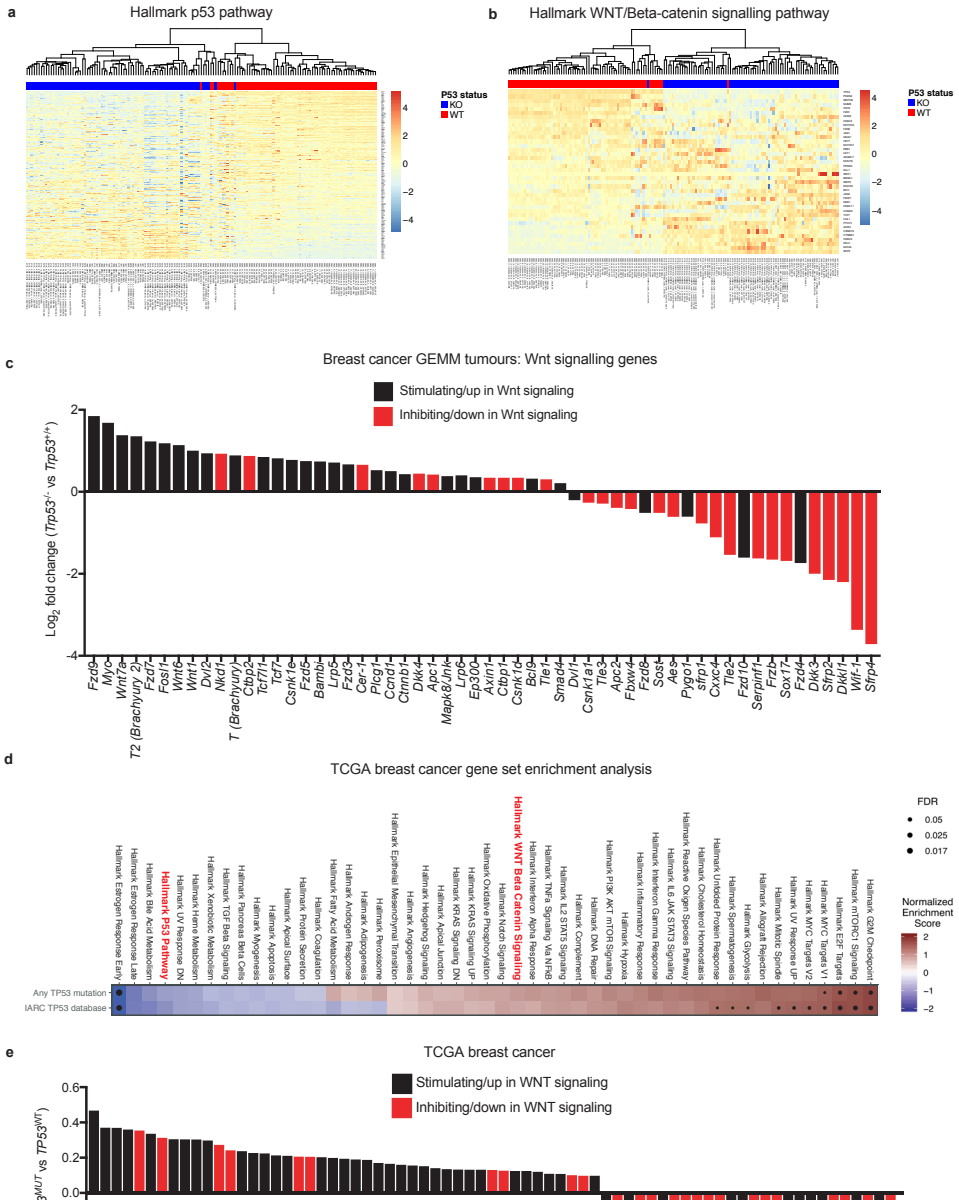
a
Hallmark p53 pathway
P53 status
KO
WT
b
Hallmark WNT/Beta-catenin signalling pathway
P53 status
KO
WT
c
Breast cancer GEMM tumours: Wnt signalling genes
Stimulating/up in Wnt signaling
Inhibiting/down in Wnt signaling
Log2 fold change (Trp53-/- vs Trp53+/+)
Fzd9
Myc
Wnt7a
T2 (Brachyury 2)
Fzd7
Fosl1
Wnt6
Wnt1
Dvl2
Nkd1
T (Brachyury)
Ctbp2
Tcf7l1
Tcf7
Csnk1e
Fzd5
Bambi
Lrp5
Fzd3
Cer-1
Plcg1
Ccnd1
Ctnnb1
Dkk4
Apc1
Mapk8/Jnk
Lrp6
Ep300
Axin1
Ctbp1
Csnk1d
Bcl9
Tle1
Smad4
Dvl1
Csnk1a1
Tle3
Apc2
Fbxw4
Fzd8
Sost
Aes
Pygo1
Sfrp1
Cxxc4
Tle2
Fzd10
Serpinf1
Fizb
Sox17
Fzd4
Dkk3
Sfrp2
Dkk1
Wif-1
Sfrp4
d
TCGA breast cancer gene set enrichment analysis
FDR
0.05
0.025
0.017
Normalized Enrichment Score
Any TP53 mutation
IARC TP53 database
Hallmark Estrogen Response Early
Hallmark Estrogen Response Late
Hallmark Bile Acid Metabolism
Hallmark P53 Pathway
Hallmark UV Response DN
Hallmark Heme Metabolism
Hallmark Xenobiotic Metabolism
Hallmark TGF Beta Signaling
Hallmark Pancreas Beta Cells
Hallmark Myogenesis
Hallmark Apoptosis
Hallmark Apical Surface
Hallmark Protein Secretion
Hallmark Coagulation
Hallmark Fatty Acid Metabolism
Hallmark Androgen Response
Hallmark Adipogenesis
Hallmark Peroxisome
Hallmark Epithelial Mesenchymal Transition
Hallmark Angiogenesis
Hallmark Hedgehog Signaling
Hallmark Apical Junction
Hallmark KRAS Signaling DN
Hallmark Oxidative Phosphorylation
Hallmark Wnt Beta Catenin Signaling
Hallmark Notch Signaling
Hallmark Interferon Alpha Response
Hallmark TNFa Signaling Via NFkB
Hallmark IL2 STAT5 Signaling
Hallmark Complement
Hallmark DNA Repair
Hallmark PI3K AKT mTOR Signaling
Hallmark Hypoxia
Hallmark Inflammatory Response
Hallmark Interferon Gamma Response
Hallmark Reactive Oxygen Species Pathway
Hallmark IL6 JAK STAT3 Signaling
Hallmark Cholesterol Homeostasis
Hallmark Unfolded Protein Response
Hallmark Spermatogenesis
Hallmark Glycolysis
Hallmark Allograft Rejection
Hallmark Mitotic Spindle
Hallmark UV Response UP
Hallmark MYC Targets V2
Hallmark MYC Targets V1
Hallmark E2F Targets
Hallmark mTORC1 Signaling
Hallmark G2M Checkpoint
e
TCGA breast cancer
Stimulating/up in WNT signaling
Inhibiting/down in WNT signaling
R value (TP53MUT vs TP53WT)
FZD9
PPP3R1
NUP1
PPARD
CSNK2A2
DVL3
DKK1
MMP7
FOSL1
TCF7L1
WNT10A
CTNNBIP1
CSNK2B
FZD1
PLCB3
PLCB4
CAMK2G
NFATC3
CSNK1E
SFRP1
FZD6
PRICKLE1
CAMK2D
WNT10B
PRKCG
FZD7
FZD5
WNT5B
MYC
BAMBI
TCF7L2
WNT2
VANGL1
ROCK2
WNT3
GSK3B
SOST
PLCB2
TCF7
RAC3
VANGL2
PRKCB
SIAH1
CSNK1E
WNT11
TCF7L1
NKD2
GPC4
SFRP4
CSNK1A1L
FZD4
CXXC4
SFRP2
FBXW11
CHD8
APC
WNT8B
LEF1
SOX17
NLK
DKK2
WNT9A
PPP3CB
WNT3
CAMK2B
AXIN2
CSNK1A1
NFATC4
SKP1
FRAT1
BTRC

Extended Data Figure 3.6. WNT-related gene activation correlates with loss of p53 in mouse and human breast tumors. a. Heatmap showing that *Trp53*$^{-/-}$ (KO) GEMM tumors (n=77) cluster away from *Trp53*$^{+/+}$ (WT) tumors (n=68) based on analysis of the Hallmark p53 pathway (represents positive control) and **b.** analysis of the Hallmark Wnt/β-catenin pathway. Analysis was performed on all tumors of Extended Data Fig. 5a. **c.** Log_2 fold change expression of genes involved in Wnt signaling ($P < 0.05$) in *Trp53*$^{-/-}$ (n=77) and *Trp53*$^{+/+}$ (n=68) GEMM tumors depicted in Extended Data Fig. 5a. Black bars indicate genes that positively regulate, or are generally increased with active Wnt signaling. Red bars indicate genes that negatively regulate, or are down-regulated with active Wnt signaling. **d.** Gene set enrichment analysis (GSEA) for Hallmark pathways in TCGA *TP53*^{WT} breast tumors (n=643) vs *TP53*^{MUT} (n=351) human tumors (any TP53 mutation) or *TP53* loss (based on the IARC TP53 database, see Materials and Methods). Normalized enrichment score is shown with False Discovery Rate (FDR) indicated. **e.** Correlation coefficient (R) of all genes involved in WNT signaling that correlate significantly ($P < 0.05$) with *TP53*^{MUT} (n=351) vs *TP53*^{WT} (n=643) in TCGA breast tumors. Black bars indicate genes that positively regulate, or are generally increased with active WNT signaling. Red bars indicate genes that negatively regulate, or are down-regulated with active WNT signaling. *P*-values were determined by two-tailed ANOVA with FDR multiple-testing correction (**c, e**).

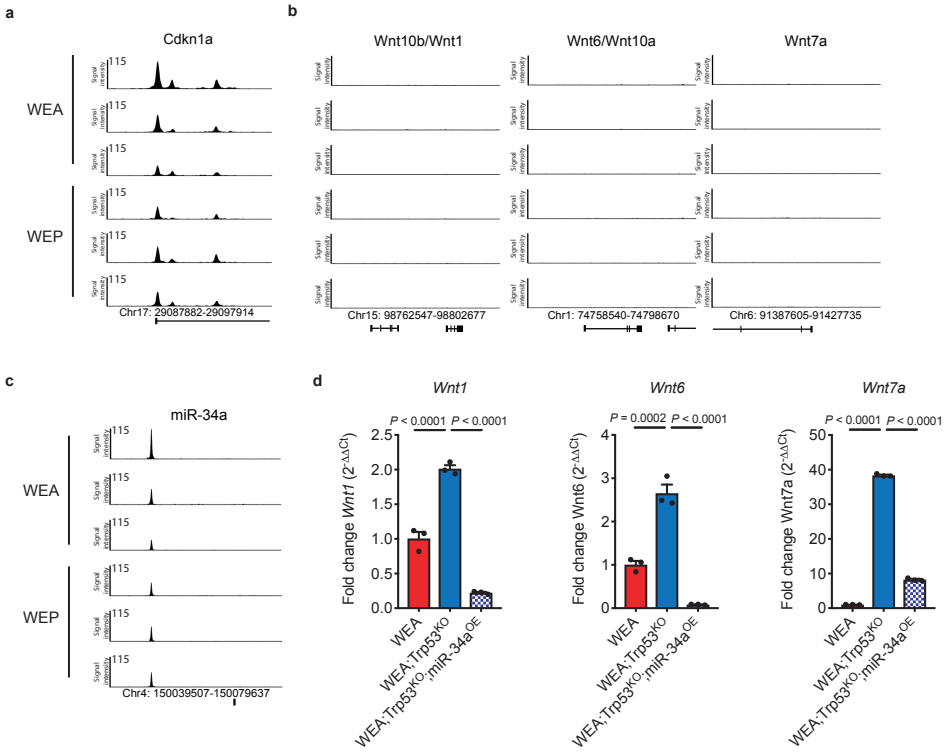

Extended Data Figure 3.7. p53 does not bind the regulatory regions of Wnt ligands directly. a. Chromatin immunoprecipitation-sequencing (ChIP-seq) profile of p53 binding to DNA demonstrating enrichment on the *Cdkn1a* (p21) locus in *Trp53*$^{+/+}$ *Wap-cre;Cdh1*$^{F/F}$*;Akt*^{E17K} (WEA) and *Wap-cre;Cdh1*$^{F/F}$*; Pik3ca*^{E545K} (WEP) cell lines (3 cell lines from 3 independent tumors per GEMM). **b.** Absence of p53 binding to *Wnt1*, *Wnt6* or *Wnt7a* loci. **c.** Enrichment of p53 on microRNA-34a (*miR-34a*) locus. **d.** RT-qPCR analysis of *Wnt* ligand expression in *WEA;Trp53*$^{+/+}$ and *WEA;Trp53*$^{-/-}$ cell lines after overexpression (OE) of miR-34a in *WEA;Trp53*$^{-/-}$ cells (n=3 technical replicates/group). Plots show representative data of 3 separate experiments with 3 technical replicates. All data are means ± s.e.m. P-values are indicated as determined by two-tailed one-way ANOVA, Tukey multiple-testing correction (**d**).

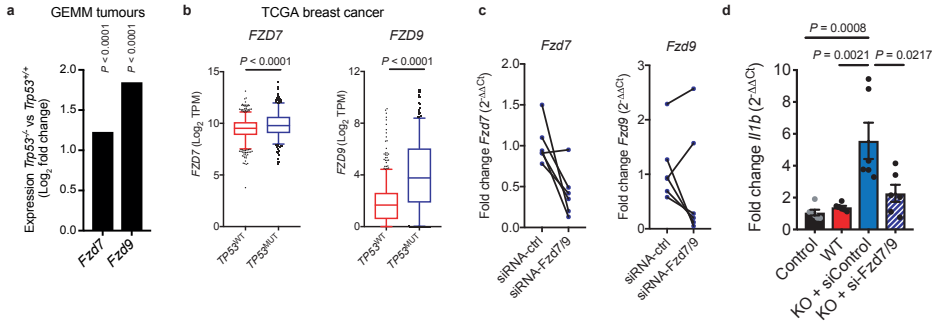

Extended Data Figure 3.8. Macrophages are activated by *Trp53*$^{-/-}$ cancer cells via Fzd7 and Fzd9 receptors *in vitro*. **a.** Log_2 fold change in expression of Wnt receptors *Fzd7* and *Fzd9* in bulk tumors comparing *Trp53*$^{-/-}$ (*n*=77) and *Trp53*$^{+/+}$ (*n*=68) GEMM tumors using RNA-sequencing. **b.** Expression of *FZD7* and *FZD9* in *TP53* wild-type (WT, *n*=643) and *TP53* mutant (MUT, *n*=351) human breast tumors of TCGA dataset. **c.** Silencing of *Fzd7* and *Fzd9* in bone marrow-derived macrophages (BMDMs) after transfection with siRNA pools against both receptors, as determined by RT-qPCR (*n*=6 biological replicates/group). **d.** Expression of *Il1b* in BMDMs after exposure to conditioned medium of *Trp53*$^{+/+}$ and *Trp53*$^{-/-}$ *Wap-cre;Cdh1*$^{F/F}$*;Akt*^{E17K} cell lines (*n*=6 biological replicates/group), as determined by RT-qPCR. Where indicated, BMDMs were transfected with control siRNA or Fzd7/9 siRNA pools. **a, c, d** show means ± s.e.m. **b.** shows 5 – 95 percentile boxplot with median and quartiles indicated. *P*-values are indicated as determined by two-tailed one-way ANOVA, FDR multiple-testing correction (**a**), two-tailed Mann-Whitney U-test (**b**) or two-tailed one-way ANOVA, Tukey multiple-testing correction (**d**).

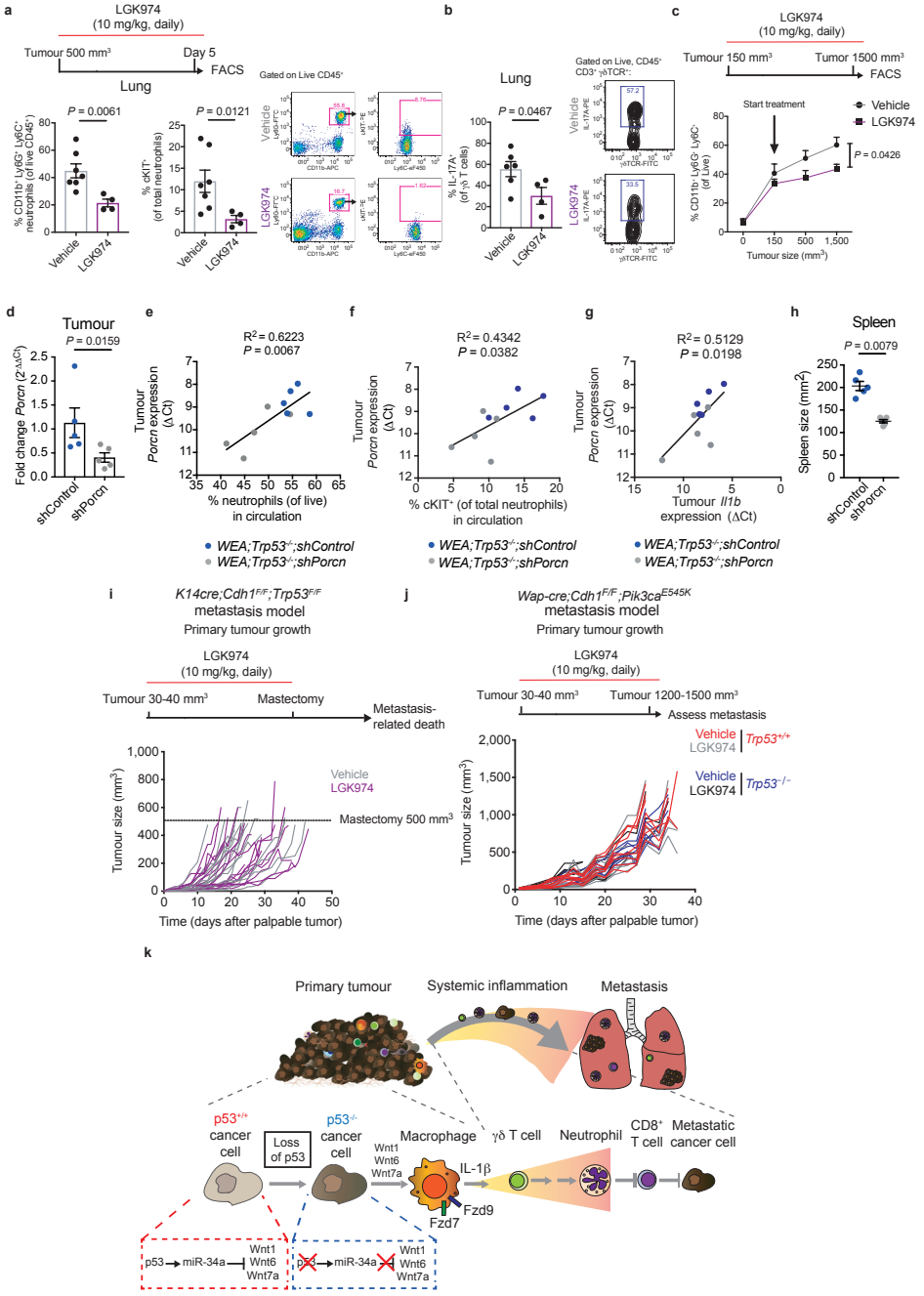
a
LGK974
(10 mg/kg, daily)
Tumour 500 mm³
Day 5
FACS
Lung
P = 0.0061
P = 0.0121
Vehicle
LGK974
b
Lung
P = 0.0467
c
LGK974
(10 mg/kg, daily)
Tumour 150 mm³
Tumour 1500 mm³
FACS
Start treatment
Vehicle
LGK974
P = 0.0426
Tumour size (mm³)
d
Tumour
P = 0.0159
shControl
shPorcn
e
R² = 0.6223
P = 0.0067
% neutrophils (of live) in circulation
f
R² = 0.4342
P = 0.0382
% cKIT⁺ (of total neutrophils) in circulation
g
R² = 0.5129
P = 0.0198
Tumour Il1b expression (ΔCt)
h
Spleen
P = 0.0079
WEA;Trp53⁻/⁻;shControl
WEA;Trp53⁻/⁻;shPorcn
i
K14cre;Cdh1F/F;Trp53F/F
metastasis model
Primary tumour growth
Tumour 30-40 mm³
Mastectomy
Metastasis-related death
Mastectomy 500 mm³
Time (days after palpable tumor)
j
Wap-cre;Cdh1F/F;Pik3caE545K
metastasis model
Primary tumour growth
Tumour 30-40 mm³
Tumour 1200-1500 mm³
Assess metastasis
Trp53+/+
Trp53−/−
k
Primary tumour
Systemic inflammation
Metastasis
p53+/+ cancer cell
Loss of p53
p53-/- cancer cell
Macrophage
γδ T cell
Neutrophil
CD8⁺ T cell
Metastatic cancer cell
Wnt1
Wnt6
Wnt7a
IL-1β
Fzd9
Fzd7
p53
miR-34a

Extended Data Figure 3.9. Pharmacological and genetic targeting of Porcupine in p53-deficient tumors reduces systemic inflammation. a. Total and cKIT+ neutrophil frequencies in lungs of vehicle (*n*=7) or LGK974 (*n*=4)-treated *K14cre;Cdh1*$^{F/F}$*;Trp53*$^{F/F}$ (KEP) mice using indicated 5 day short-term treatment schedule. Representative flow cytometry plots are shown. **b.** Frequency of IL-17A-producing γδ T cells in lungs of vehicle (*n*=6) or LGK974 (*n*=4)-treated KEP mice. Representative flow cytometry plots are shown. **c.** Kinetics of circulating neutrophils in vehicle or LGK974-treated KEP mice using indicated long-term treatment schedule, shown as frequency at indicated tumor volumes (*n*=8/group). **d.** RT-qPCR analysis of *Porcn* expression in end-stage bulk tumor (*n*=5/group). Data are normalized to *shControl* and represents an average of 2 technical replicates. **e.** Correlation of total neutrophil levels in circulation with expression of *Porcn* in *WEA;Trp53*$^{-/-}$*;shControl* and *WEA;Trp53*$^{-/-}$*;shPorcn* whole tumor lysate (*n*=5/group). **f.** Correlation of cKIT+ neutrophil levels in circulation with expression of *Porcn* in *WEA;Trp53*$^{-/-}$*;shControl* and *WEA;Trp53*$^{-/-}$*;shPorcn* whole tumor lysate (*n*=5/group). **g.** Correlation of *Porcn* expression and *Il1b* expression in bulk *WEA;Trp53*$^{-/-}$*;shControl* (blue) and *WEA;Trp53*$^{-/-}$*;shPorcn* tumors (grey) (*n*=5/group). Data represent an average of 2 technical replicates. **h.** Spleen area in mice with *WEA;Trp53*$^{-/-}$*;shControl* (blue) and *WEA;Trp53*$^{-/-}$*;shPorcn* tumors (grey) tumors at end-stage (*n*=5/group). **i.** Growth kinetics of orthotopically transplanted KEP mammary tumors, treated with vehicle (*n*=12) or LGK974 (*n*=15). Each line represents an individual mouse. **j.** Growth kinetics of orthotopically injected *Trp53*$^{+/+}$ and *Trp53*$^{-/-}$ *Wap-cre;Cdh1*$^{F/F}$*;Pik3ca*^{E545K} (WEP) cells, treated with vehicle or LGK974. Each line represents an individual mouse (*n*=9/group). **k.** Schematic representation of the findings of this study: loss of p53 in breast cancer cells triggers secretion of Wnt ligands to activate tumor-associated macrophages. This stimulates systemic expansion and activation of neutrophils, which we have previously shown to be immunosuppressive [5], thus driving metastasis. All data are means ± s.e.m. *P*-values are indicated as determined by two-tailed Mann-Whitney U-test (**a – d, h**), linear regression analysis (**e – g**) and area under the curve of average growth curves, followed by two-tailed Welch's t-test (**i, j**).

Supplemental Table 3.1. List of antibodies used for flow cytometry, western blotting, immunohistochemistry and chromatin immunoprecipitation.

Flow cytometry

Antigen	Fluorochrome	Clone	Company	Catalogue number	Dilution
CD45	eFluor 605NC	30-F11	eBioscience/ThermoFisher	93-0451	1:100
	BUV395		BD Biosciences	564279	1:200
CD11b	BV650	M1/70	BioLegend	101239	1:400
	APC		eBioscience/ThermoFisher	17-0112-81	
	APC-eFluor 780			47-0112-82	
Ly6G	APC	1A8	eBioscience/ThermoFisher	17-9668-82	1:400
	FITC		BD Biosciences	561105	
Ly6C	eFluor 450	HK1.4	eBioscience/ThermoFisher	48-5932-82	1:400
F4/80	APC-eFluor 780	BM8	eBioscience/ThermoFisher	47-4801-82	1:400
	APC			17-4801-82	
	FITC			11-4801-82	
cKIT	PE	2B8	eBioscience/ThermoFisher	12-1171-82	1:200
	PE-Cy7			25-1171-82	
CD3	PE-Cy7	145-2C11	eBioscience/ThermoFisher	25-0031-82	1:200
CD4	APC-eFluor 780	GK1.5	eBioscience/ThermoFisher	47-0041-82	1:200
CD8	APC-eFluor 780	53-6.7	eBioscience/ThermoFisher	47-0081-82	1:400
	PerCP-eFluor 710			46-0081-82	
γδ TCR	FITC	GL3	BD Biosciences	553177	1:400
CD19	APC-eFluor 780	eBio1D3	eBioscience/ThermoFisher	47-0193-82	1:200
CD34	eFluor 450	RAM34	eBioscience/ThermoFisher	48-0341-82	1:100
CD16/32	PerCP-eFluor 710	93	eBioscience/ThermoFisher	46-0161-82	1:200
Sca-1	PE	D7	eBioscience/ThermoFisher	12-5981-82	1:100
CD45R	APC-eFluor 780	RA3-6B2	eBioscience/ThermoFisher	47-0452-82	1:200
CD5	APC-eFluor 780	53-7.3	eBioscience/ThermoFisher	47-0051-82	1:200
CD127	APC-eFluor 780	A7R34	eBioscience/ThermoFisher	47-1271-82	1:200
Ter119	APC-eFluor 780	TER-119	eBioscience/ThermoFisher	47-5921-82	1:200
CCR2	AF700	475301	R&D Systems	FAB5538N	1:200
CCR6	BV421	29-2L17	BioLegend	129817	1:200
CD206	AF488	MR5D3	AbD Serotec/Bio-Rad	MCA2235	1:200
CSF-1R	PE	AFS98	eBioscience/ThermoFisher	12-1152-82	1:200
CXCR4	PerCP-eFluor 710	2B11	eBioscience/ThermoFisher	46-9991-82	1:200
MHC-II	APC-eFluor 780	M5/114.15.2	eBioscience/ThermoFisher	47-5321-82	1:200
CD68	BV421	Y1/82A	BD Biosciences	564943	1:200
CD14	BUV737	M5E2	BD Biosciences	564444	1:400
CD206	FITC	15-2	BioLegend	321103	1:200
CD168	APC	GHI/61	BioLegend	333609	1:200
HLA-DR	BV650	G46-6	BD Biosciences	564231	1:200

Supplemental Table 3.1. List of antibodies used for flow cytometry, western blotting, immunohistochemistry and chromatin immunoprecipitation (continued).

Western blotting

Antigen	Fluorochrome	Clone	Company	Catalogue number	Dilution
p53	-	1C12	Cell Signaling	2524	1:1000
p21	-	SX118	BD Biosciences	556430	1:1000
WNT1	-	10C8	EMD Millipore	MABD168	1:1000
WNT6	-	Polyclonal (EPR9244)	Abcam	Ab154144	1:1000
WNT7a	-	Polyclonal	Novus Biologicals	NBP2-20913	1:1000
Porcupine		Polyclonal	Novus Biologicals	NBP1-79322	1:1000
Non-phospho-β-catenin	-	8E7	EMD Millipore	05-665	1:1000
β-actin	-	D6A8 A1978	Cell Signaling Sigma	8457 A2228	1:5000 1:5000
GAPDH	-	6C5	HyTest	5G4	1:5000
Donkey-anti-mouse IgG	IRDye 680RD		LiCor	926-68072	1:10000
Donkey-anti-rabbit IgG	IRDye 800CW		LiCor	926-32213	1:10000

Immunohistochemistry

Antigen	Antigen retrieval	Clone	Company	Catalogue number	Dilution
Ly6G	Proteinase K 20 µg/ml	1A8	BD Biosciences	551459	1:150
F4/80	Proteinase K 20 µg/ml	CI:A3-1	AbD Serotec/Bio-Rad	MCA497GA	1:400
CD8	Tris/EDTA pH 9.0	4SM15	eBioscience/ThermoFisher	14-0808-82	1:2000
CD4	Tris/EDTA pH 9.0	4SM95	eBioscience/ThermoFisher	14-9766-82	1:1000
Foxp3	Citrate buffer	FJK-16s	eBioscience/ThermoFisher	14-5773-82	1:400
Cytokeratin-8	Citrate buffer	Troma-I	DSHB University of Iowa	TROMA-I	1:600
Goat-anti-Rat IgG	-	3052-08	SouthernBiotech	3052-08	1:100

Chromatin immunoprecipitation

Antigen	Amount used	Clone	Company	Catalogue number
p53	5 µg	1C12	Cell Signaling	2524

Supplemental Table 3.2. RT-qPCR primers.

Mouse

Gene	Forward (5' – 3')	Reverse (5' – 3')
Wnt1	GAACCCTTTTGCCATCCTGA	CACCTTCAAGAGTTGACCTC
Wnt6	GCA GACTGGGG GTTCGAG	CCTGACAACCACACTGTAGGAG
Wnt7a	GGCTTCTCTTCGGTGGTAGC	TGAAACTGACACTCGTCCAGG
Il1b	CAACCAACAAGTGATATTCTCCATG	GATCCACACTCTCCAGCTGCA
Porcn	TGGAGTTCATGGGCTACCTCT	CGTTTCTTGTTGCGAAGGAGT
Actb	CCTCATGAAGATCCTGACCGA	TTTGATGTCACGCACGATTTC
Gapdh	AGGTCGGTGTGAACGGATTTG	TGTAGACCATGTAGTTGAGGTCA

Human

Gene	Forward (5' – 3')	Reverse (5' – 3')
IL1B	AATCTGTACCTGTCCTGCGTGTT	TGGGTAATTTTTGGGATCTACACTCT
ACTB	CATGTACGTTGCTATCCAGGC	CTCCTTAATGTCACGCACGAT

References

1 Diakos, C. I., Charles, K. A., McMillan, D. C. & Clarke, S. J. Cancer-related inflammation and treatment effectiveness. *Lancet Oncol.* **15**, e493-503, doi:10.1016/S1470-2045(14)70263-3 (2014).

2 McAllister, S. S. & Weinberg, R. A. The tumour-induced systemic environment as a critical regulator of cancer progression and metastasis. *Nat. Cell Biol.* **16**, 717-727, doi:10.1038/ncb3015 (2014).

3 Templeton, A. J. *et al.* Prognostic role of neutrophil-to-lymphocyte ratio in solid tumors: a systematic review and meta-analysis. *J. Natl. Cancer Inst.* **106**, dju124, doi:10.1093/jnci/dju124 (2014).

4 Coffelt, S. B., Wellenstein, M. D. & de Visser, K. E. Neutrophils in cancer: neutral no more. *Nat. Rev. Cancer* **16**, 431–446, doi:10.1038/nrc.2016.52 (2016).

5 Coffelt, S. B. *et al.* IL-17-producing gammadelta T cells and neutrophils conspire to promote breast cancer metastasis. *Nature* **522**, 345–348, doi:10.1038/nature14282 (2015).

6 Kowanetz, M. *et al.* Granulocyte-colony stimulating factor promotes lung metastasis through mobilization of Ly6G+Ly6C+ granulocytes. *Proc. Natl. Acad. Sci. U. S. A.* **107**, 21248-21255, doi:10.1073/pnas.1015855107 (2010).

7 Bald, T. *et al.* Ultraviolet-radiation-induced inflammation promotes angiotropism and metastasis in melanoma. *Nature* **507**, 109-113, doi:10.1038/nature13111 (2014).

8 Wculek, S. K. & Malanchi, I. Neutrophils support lung colonization of metastasis-initiating breast cancer cells. *Nature* **528**, 413–417 (2015).

9 Park, J. *et al.* Cancer cells induce metastasis-supporting neutrophil extracellular DNA traps. *Sci. Transl. Med.* **8**, 361ra138, doi:10.1126/scitranslmed.aag1711 (2016).

10 Steele, C. W. *et al.* CXCR2 Inhibition Profoundly Suppresses Metastases and Augments Immunotherapy in Pancreatic Ductal Adenocarcinoma. *Cancer Cell* **29**, 832-845, doi:10.1016/j.ccell.2016.04.014 (2016).

11 Ethier, J. L., Desautels, D., Templeton, A., Shah, P. S. & Amir, E. Prognostic role of neutrophil-to-lymphocyte ratio in breast cancer: a systematic review and meta-analysis. *Breast Cancer Res.* **19**, 2, doi:10.1186/s13058-016-0794-1 (2017).

12 Cooks, T. *et al.* Mutant p53 prolongs NF-kappaB activation and promotes chronic inflammation and inflammation-associated colorectal cancer. *Cancer Cell* **23**, 634-646, doi:10.1016/j.ccr.2013.03.022 (2013).

13 Schwitalla, S. *et al.* Loss of p53 in enterocytes generates an inflammatory microenvironment enabling invasion and lymph node metastasis of carcinogen-induced colorectal tumors. *Cancer Cell* **23**, 93-106, doi:10.1016/j.ccr.2012.11.014 (2013).

14 Stodden, G. R. *et al.* Loss of Cdh1 and Trp53 in the uterus induces chronic inflammation with modification of tumor microenvironment. *Oncogene* **34**, 2471-2482, doi:10.1038/onc.2014.193 (2015).

15 Wörmann, S. M. *et al.* Loss of P53 Function Activates JAK2-STAT3 Signaling to Promote Pancreatic Tumor Growth, Stroma Modification, and Gemcitabine Resistance in Mice and is Associated With Patient Survival. *Gastroenterology* **151**, 180-193, doi:10.1053/j.gastro.2016.03.010 (2016).

16 Bezzi, M. *et al.* Diverse genetic-driven immune landscapes dictate tumor progression through distinct mechanisms. *Nat. Med.* **24**, 165-175, doi:10.1038/nm.4463 (2018).

17 Kersten, K. *et al.* Mammary tumor-derived CCL2 enhances pro-metastatic systemic inflammation through upregulation of IL1beta in tumor-associated macrophages. *Oncoimmunology* **6**, e1334744, doi:10.1080/2162402X.2017.1334744 (2017).

18 Annunziato, S. *et al.* Modeling invasive lobular breast carcinoma by CRISPR/Cas9-mediated somatic genome editing of the mammary gland. *Genes Dev.* **30**, 1470-1480, doi:10.1101/gad.279190.116 (2016).

19 Song, X. *et al.* CD11b+/Gr-1+ immature myeloid cells mediate suppression of T cells in mice bearing tumors of IL-1beta-secreting cells. *J. Immunol.* **175**, 8200-8208 (2005).

20 Singh, V., Holla, S., Ramachandra, S. G. & Balaji, K. N. WNT-inflammasome signaling mediates NOD2-induced development of acute arthritis in mice. *J. Immunol.* **194**, 3351-3360, doi:10.4049/jimmunol.1402498 (2015).

21 Spranger, S., Bao, R. & Gajewski, T. F. Melanoma-intrinsic beta-catenin signalling prevents

anti-tumour immunity. *Nature* **523**, 231-235, doi:10.1038/nature14404 (2015).
22 Avgustinova, A. *et al.* Tumour cell-derived Wnt7a recruits and activates fibroblasts to promote tumour aggressiveness. *Nat. Commun.* **7**, 10305, doi:10.1038/ncomms10305 (2016).
23 Luke, J. J., Bao, R., Sweis, R. F., Spranger, S. & Gajewski, T. F. WNT/beta-catenin pathway activation correlates with immune exclusion across human cancers. *Clin. Cancer Res.*, doi:10.1158/1078-0432.CCR-18-1942 (2019).
24 Kim, N. H. *et al.* p53 and microRNA-34 are suppressors of canonical Wnt signaling. *Sci. Signal.* **4**, ra71, doi:10.1126/scisignal.2001744 (2011).
25 Nusse, R. & Clevers, H. Wnt/beta-Catenin Signaling, Disease, and Emerging Therapeutic Modalities. *Cell* **169**, 985-999, doi:10.1016/j.cell.2017.05.016 (2017).
26 Wellenstein, M. D. & de Visser, K. E. Cancer-Cell-Intrinsic Mechanisms Shaping the Tumor Immune Landscape. *Immunity* **48**, 399–416, doi:10.1016/j.immuni.2018.03.004 (2018).
27 Boggio, K., Nicoletti, G., Di Carlo, E., Cavallo, F., Landuzzi, L., Melani, C., Giovarelli, M., Rossi, I., Nanni, P., De Giovanni, C., Bouchard, P., Wolf, S., Modesti, A., Musiani, P., Lollini, P.L., Colombo, M.P., Forni, G. Interleukin 12–mediated Prevention of Spontaneous Mammary Adenocarcinomas in Two Lines of Her-2/neu Transgenic Mice. *J. Exp. Med.* **188**, 589-596, doi:10.1084/jem.188.3.589 (1998).
28 Jonkers, J. *et al.* Synergistic tumor suppressor activity of BRCA2 and p53 in a conditional mouse model for breast cancer. *Nat. Genet.* **29**, 418-425, doi:10.1038/ng747 (2001).
29 Derksen, P. W. *et al.* Somatic inactivation of E-cadherin and p53 in mice leads to metastatic lobular mammary carcinoma through induction of anoikis resistance and angiogenesis. *Cancer Cell* **10**, 437-449, doi:10.1016/j.ccr.2006.09.013 (2006).
30 Liu, X. *et al.* Somatic loss of BRCA1 and p53 in mice induces mammary tumors with features of human BRCA1-mutated basal-like breast cancer. *Proc Natl Acad Sci U S A* **104**, 12111-12116, doi:10.1073/pnas.0702969104 (2007).
31 Henneman, L. *et al.* Selective resistance to the PARP inhibitor olaparib in a mouse model for BRCA1-deficient metaplastic breast cancer. *Proc. Natl. Acad. Sci. U.S.A.* **112**, 8409-8414, doi:10.1073/pnas.1500223112 (2015).
32 Huijbers, I. J. *et al.* Using the GEMM-ESC strategy to study gene function in mouse models. *Nat. Protoc.* **10**, 1755-1785, doi:10.1038/nprot.2015.114 (2015).
33 Kas, S. M. *et al.* Insertional mutagenesis identifies drivers of a novel oncogenic pathway in invasive lobular breast carcinoma. *Nat. Genet.* **49**, 1219-1230, doi:10.1038/ng.3905 (2017).
34 Annunziato, S. *et al.* Comparative oncogenomics identifies combinations of driver genes and drug targets in BRCA1-mutated breast cancer. *Nat. Commun.* **10**, 397, doi:10.1038/s41467-019-08301-2 (2019).
35 Liu, J. *et al.* Targeting Wnt-driven cancer through the inhibition of Porcupine by LGK974. *Proc. Natl. Acad. Sci. U.S.A.* **110**, 20224-20229, doi:10.1073/pnas.1314239110 (2013).
36 Doornebal, C. W. *et al.* A preclinical mouse model of invasive lobular breast cancer metastasis. *Cancer Res.* **73**, 353-363, doi:10.1158/0008-5472.CAN-11-4208 (2013).
37 Sanjana, N. E., Shalem, O. & Zhang, F. Improved vectors and genome-wide libraries for CRISPR screening. *Nat. Methods* **11**, 783-784, doi:10.1038/nmeth.3047 (2014).
38 Brinkman, E. K., Chen, T., Amendola, M. & van Steensel, B. Easy quantitative assessment of genome editing by sequence trace decomposition. *Nucleic Acids Res.* **42**, e168, doi:10.1093/nar/gku936 (2014).
39 Schmidt, D. *et al.* ChIP-seq: using high-throughput sequencing to discover protein-DNA interactions. *Methods* **48**, 240-248, doi:10.1016/j.ymeth.2009.03.001 (2009).
40 Lerdrup, M., Johansen, J. V., Agrawal-Singh, S. & Hansen, K. An interactive environment for agile analysis and visualization of ChIP-sequencing data. *Nat. Struct. Mol. Biol.* **23**, 349-357, doi:10.1038/nsmb.3180 (2016).
41 Okada, N. *et al.* A positive feedback between p53 and miR-34 miRNAs mediates tumor suppression. *Genes Dev.* **28**, 438-450, doi:10.1101/gad.233585.113 (2014).
42 Kim, D. *et al.* TopHat2: accurate alignment of transcriptomes in the presence of insertions, deletions and gene fusions. *Genome Biol.* **14**, R36, doi:10.1186/gb-2013-14-4-r36 (2013).
43 Trapnell, C., Pachter, L. & Salzberg, S. L. TopHat: discovering splice junctions with RNA-Seq. *Bioinformatics* **25**, 1105-1111, doi:10.1093/bioinformatics/btp120 (2009).
44 Anders, S., Pyl, P. T. & Huber, W. HTSeq--a Python framework to work with high-throughput sequencing data. *Bioinformatics* **31**, 166-169, doi:10.1093/bioinformatics/btu638 (2015).

45 Robinson, M. D., McCarthy, D. J. & Smyth, G. K. edgeR: a Bioconductor package for differential expression analysis of digital gene expression data. *Bioinformatics* **26**, 139-140, doi:10.1093/bioinformatics/btp616 (2010).
46 Law, C. W., Chen, Y., Shi, W. & Smyth, G. K. voom: Precision weights unlock linear model analysis tools for RNA-seq read counts. *Genome Biol.* **15**, R29, doi:10.1186/gb-2014-15-2-r29 (2014).
47 Liberzon, A. *et al.* The Molecular Signatures Database (MSigDB) hallmark gene set collection. *Cell Syst.* **1**, 417-425, doi:10.1016/j.cels.2015.12.004 (2015).
48 Bouaoun, L. *et al.* TP53 Variations in Human Cancers: New Lessons from the IARC TP53 Database and Genomics Data. *Hum. Mutat.* **37**, 865-876, doi:10.1002/humu.23035 (2016).